One Attention, One Scale: Phase-Aligned Rotary Positional Embeddings for Mixed-Resolution Diffusion Transformer

Haoyu Wu¹ Jingyi Xu¹ Qiaomu Miao¹ Dimitris Samaras¹ Hieu Le²

¹Stony Brook University ²UNC-Charlotte

Abstract

We identify a core failure mode that occurs when using the usual linear interpolation on rotary positional embeddings (RoPE) for mixed-resolution denoising with Diffusion Transformers. When tokens from different spatial grids are mixed, the attention mechanism collapses. The issue is structural. Linear coordinate remapping forces a single attention head to compare RoPE phases sampled at incompatible rates, creating phase aliasing that destabilizes the score landscape. Pretrained DiTs are especially brittle—many heads exhibit extremely sharp, periodic phase selectivity—so even tiny cross-rate inconsistencies reliably cause blur, artifacts, or full collapse.

To this end, our main contribution is Cross-Resolution Phase-Aligned Attention (CRPA), a training-free drop-in fix that eliminates this failure at its source. CRPA modifies only the RoPE index map for each attention call: all Q/K positions are expressed on the query's stride so that equal physical distances always induce identical phase increments. This restores the precise phase patterns that DiTs rely on. CRPA is fully compatible with pretrained DiTs, stabilizes all heads and layers uniformly. We demonstrate that CRPA enables high-fidelity and efficient mixed-resolution generation, outperforming previous state-of-the-art methods on image and video generation.

1. Introduction

Rotary Positional Embeddings [97] (RoPE) have become the standard positional encoding in modern Transformers, from large language models [2, 4, 16, 25, 33, 100, 101, 105, 123] to diffusion generators [19, 31, 34, 53, 68, 103, 109, 120, 134]. Their rotation-based formulation encodes positions in a way that naturally preserves relative offsets, allowing attention heads to compare tokens by their spatial or temporal differences without relying on fixed absolute indices [106]. This relative inductive bias is simple, parameter-free, and works reliably across architectures [3, 36, 87, 93, 111, 114, 115], which is why RoPE is now widely adopted.

Prompt: "A cat walks on the grass, realistic."

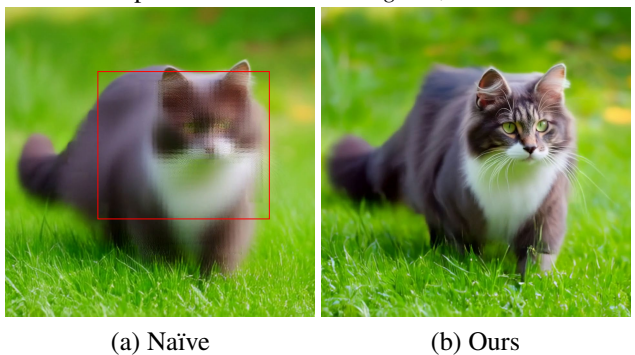


Figure 1. **Mixed-Resolution Denoising.** (a) Naïve mixed-resolution denoising, with the high-resolution region outlined in red, collapses due to RoPE [97] phase mismatches between resolutions, producing severe blur and instability. (b) Our Cross-Resolution Phase-Aligned Attention (CRPA) keeps RoPE phases synchronized across scales, restoring sharp and consistent detail.

We study how RoPE behaves when attention spans tokens at different spatial resolutions, a scenario that naturally arises in mixed-resolution denoising for efficient generation [42]. A straightforward approach is to linearly interpolate or remap positional indices so that high- and lowresolution tokens share a unified coordinate system before applying attention [13]. In practice, this strategy breaks down (Fig. 1). The issue is a scale mismatch: a single attention operation now mixes tokens whose positions were sampled at different spatial densities. RoPE interprets position through phase increments $\theta_i = \omega_i p$, so the same physical offset produces different phase steps depending on the underlying sampling rate. When these mismatched phases are combined inside one attention head, tiny spatial shifts can inflate into large angular discrepancies, destabilizing attention and leading to blur or collapse.

We verify this in our diagnosis. Probing pretrained DiTs shows that many attention heads are strongly sensitive to specific phase: activations exhibit clear periodic structure with a sharp peak at very small relative distances ($\Delta \approx 0$).

 $^{^1\}text{RoPE}$ maps a position p to a rotation angle ("phase") $\theta_i=\omega_i p$ for each sinusoidal frequency $\omega_i.$

The effect is amplified in heads that rely more on positional cues than on content [15], and it remains stable across diffusion timesteps. These properties make mixed-resolution attention particularly brittle when phases are compared across incompatible sampling scales, which is a setting that has not yet been fully explored in prior work on RoPE interpolation and extrapolation [13, 21, 76, 78, 79, 83, 98, 122, 129].

Motivated by these observations, we propose Cross-Resolution Phase-Aligned Attention (CRPA), a training-free mechanism that enforces a principle: one attention, one scale. Before each query–key–value dot product, all positions are expressed on a single reference grid determined by the query. In other words, key/value tokens are resampled in index space to the query's units so that equal physical distances correspond to equal phases within that computation. This keeps phases coherent across resolutions and removes the cross-rate aliasing that arises from naïve interpolation.

While CRPA stabilizes attention, boundaries where the resolution changes can still exhibit small content or texture mismatches. We therefore introduce a lightweight Boundary Expand-and-Replace step that operates in a small overlapping band around each boundary: within this band, features are softly exchanged between the low- and high-resolution sides via latent-space up/downsampling, improving local consistency.

Finally, we place these components in a practical denoising schedule that proceeds from coarse to mixed (and optionally to full resolution for the last steps). This design preserves global structure, allocates computation to critical regions, and yields high visual fidelity at reduced cost for both images and videos.

In summary, our contributions are:

- We provide an intuitive and quantitative analysis of why linear RoPE interpolation fails under mixed resolution in DiTs, identifying scale-induced phase mismatch as the driver of cross-rate aliasing and instability.
- We introduce Cross-Resolution Phase-Aligned Attention (CRPA), which maintains RoPE coherence by expressing all phases on the query's scale within each attention computation.
- We propose a lightweight Boundary Expand-and-Replace procedure that harmonizes textures and densities near resolution transitions.

Together, these components enable stable, high-fidelity, and efficient mixed-resolution generation for images and videos.

2. Related Work

Diffusion Transformers (DiTs). Replacing U-Nets with Transformer has proven highly scalable for diffusion models, with DiTs operating on latent patches and achieving state-of-the-art generation [77]. Multimodal variants further improve text–image/video alignment and visual fidelity

[9, 26, 29, 34, 53, 54, 57, 74, 82, 99, 109, 118, 132]. We study DiT efficiency under mixed resolutions, focusing on stability when attention spans tokens from heterogeneous grids.

Positional Encoding. A key choice in DiTs is the positional encoding used in self-attention. RoPE [97] rotates queries and keys using frequency-based phases and is now standard across vision and language transformers [15, 36, 68, 134]. Work on extending RoPE beyond its trained context—linear interpolation, NTK-aware scaling, YaRN—targets long-range extrapolation [13, 21, 78, 79]. Trainable or Lie-group generalizations [76, 122] aim to improve robustness across resolutions, while alternatives like ALiBi [83], XPos [98], and other relative schemes pursue greater stability. However, prior efforts concentrate on 1D language sequences or long-context vision tokens [129], not on mixed-resolution denoising where tokens come from incompatible spatial grids.

Mixed-Resolution Denoising. Coarse-to-fine and multistage diffusion pipelines reduce compute while maintaining fidelity, often operating in VAE latents [88]. Two-stage and cascaded systems are common [14, 24, 38, 45, 80, 81, 89, 102]. RALU [42] adopts a three-stage schedule that upsamples artifact-prone regions with noise-timestep rescheduling, but it ignores RoPE phase mismatch across resolutions and compensates with extra noise and steps. Other approaches explore high—low—high strategies [104], regionadaptive sampling [63], latent-space super-resolution [41], and patch-based schemes [22]. Our work follows the coarse-to-fine paradigm but directly tackles attention collapse during mixed-resolution inference, enabling stable low—mixed—full-resolution generation.

Diffusion Acceleration. Many acceleration methods reduce either step count or per-step compute and are orthogonal to our focus. Token-reduction techniques merge, prune, or route tokens to lower cost with minimal degradation [6, 8, 12, 121, 124, 125]. Model-compression approaches—quantization [10, 20, 55, 92], distillation [30, 56, 126], block pruning [28, 72, 91], and structured or unstructured pruning [7, 27, 32, 108, 128]—trade capacity for efficiency. Feature-caching methods reuse hidden states across steps [1, 11, 46, 61, 70, 72, 73, 116, 135], sometimes with selective token routing [63, 65, 121]. Sampler advancements cut step counts without retraining [66, 67, 95, 130, 131], and progressive distillation or consistency models push toward few- or one-step generation [69, 90, 96].

3. Understanding RoPE Interpolation Failures in Mixed-Resolution Denoising

In this section, we study why linear position interpolation for RoPE collapses for DiTs under mixed-resolution denoising. Through controlled counterexamples and head-wise measurements, we show that pretrained attention heads are phase sensitive to the relative distance Δ encoded by RoPE: activations exhibit sharp decay around $\Delta\approx 0$ and strong periodicity. Interpolating positions across sampling rates therefore introduces cross-rate phase mismatch and effective aliasing, which destabilizes generation.

3.1. Preliminary - RoPE

We first recall a simple case of RoPE in 1D. Let an attention head have even dimensionality d, and let ω_i denote the i-th angular frequency, typically a geometric sequence: $\omega_i = 10000^{-2i/d}, \ i \in \{0,1,\ldots,d/2-1\}$. For a scalar position $p \in \mathbb{R}$, RoPE rotates each (2i,2i+1) pair by angle $\theta_i(p) = \omega_i p$:

$$R(\theta) = \begin{bmatrix} \cos \theta & -\sin \theta \\ \sin \theta & \cos \theta \end{bmatrix},\tag{1}$$

$$\mathcal{R}(p) = \operatorname{diag}(R(\theta_0(p)), \dots, R(\theta_{d/2-1}(p))). \tag{2}$$

Given tokens $q, k \in \mathbb{R}^d$, RoPE applies $q \to \mathcal{R}(p_q)q, k \to \mathcal{R}(p_k)k$. The attention score obeys the relative property

$$(\mathcal{R}(p_q)q)^{\top}(\mathcal{R}(p_k)k) = q^{\top}\mathcal{R}(\Delta) k, \qquad (3)$$

i.e., RoPE converts absolute positions to a frequency-coded phase that depends only on the relative offset $\Delta = p_k - p_q$. **Extension to 2D/3D.** For images/videos, positions are tuples $p = (p^h, p^w)$ or (p^t, p^h, p^w) . Standard practice assigns disjoint coordinate pairs (or channel groups) to each axis and uses separable rotations: $\mathcal{R}(p) = \mathcal{R}_h(p^h) \oplus \mathcal{R}_w(p^w)$ (and $\oplus \mathcal{R}_t(p^t)$ for video).

3.2. Linear Interpolation of RoPE

Mixed-resolution denoising can, in principle, accelerate DiT inference by allocating high resolution to salient regions and lower resolution elsewhere. However, this setting remains largely unexplored, particularly regarding how RoPE behaves when attention spans tokens sampled at different spatial rates. A natural starting point is linear position interpolation (PI) [13], which is widely used in language models, vision transformers, and DiTs. Thus, we adopt linear interpolation as the baseline for mapping LR and HR tokens into a unified positional space.

For clarity, we consider a simplified 1D example (the actual model operates on 2D image or 3D video tokens). Starting from indices [0, 1, 2, 3, 4, 5, 6, 7, 8], suppose the middle segment [3, 4] is upsampled into a high-resolution block. We then analyze two straightforward strategies for aligning the low-resolution (LR) and high-resolution (HR) regions:

(i) Fractional unification (LR grid with fractional HR indices).

$$\underbrace{0\ 1\ 2}_{LR}\ \underbrace{3.0\ 3.5\ 4.0\ 4.5}_{HR}\ \underbrace{5\ 6\ 7\ 8}_{LR}.$$

Prompt: "Hyper-realistic spaceship landing on Mars."

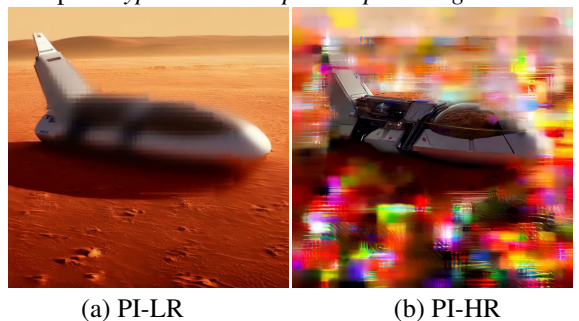


Figure 2. Results for RoPE with linear position [13] interpolation (PI) to the low- or high-resolution grid.

(ii) Integerized unification (warp LR zones to keep integer indices). Here, LR zones are stretched by 2 while the HR block remains dense:

$$\underbrace{0\ 2\ 4}_{LR}\ \underbrace{6\ 7\ 8\ 9}_{HR}\ \underbrace{10\ 12\ 14\ 16}_{LR}.$$

Formally, We unify two schemes via a piecewise-affine map applied to RoPE positions p:

$$\phi(p) = a_r + s_r (p - b_r), \qquad p \in r, \tag{4}$$

where r represents the region (LR or HR), s_r is the perregion scale factor, b_r is the region's original start index, and a_r ensures continuity across boundaries. However, in Fig. 2, we observe both schemes lead to systematic failures in generation: one preserves plausibility in the LR region while causing the HR region to collapse, and the other does the opposite. To understand this failure mode, we analyze how relative distance governs the attention output in the next section.

3.3. Attention Scores vs. Relative Distance (Δ)

To understand why linear RoPE interpolation destabilizes mixed-resolution attention, we directly probe how pretrained DiT attention heads respond to *relative positional offsets*. RoPE rewrites the attention score in terms of a phase shift determined solely by the offset $\Delta=p_k-p_q.$ If attention heads rely on these phases in a structured way, then sampling Δ inconsistently across LR and HR grids will directly corrupt their inputs. Our goal is therefore to characterize the learned dependence of attention scores on $\Delta.$

Measuring head response. During diffusion inference, we randomly sample tokens from the model's forward pass to form (q, k) pairs. For each pair, we compute the cosine similarity between the query and the RoPE-rotated key:

$$\kappa(\Delta) := \mathbb{E}_{(q,k)} \left[\langle \widehat{q}, \mathcal{R}(\Delta) \widehat{k} \rangle \right], \tag{5}$$

where hats denote ℓ_2 -normalization. This measurement isolates the head's dependence on relative distance, independent of actual token content. We aggregate $\kappa(\Delta)$ across

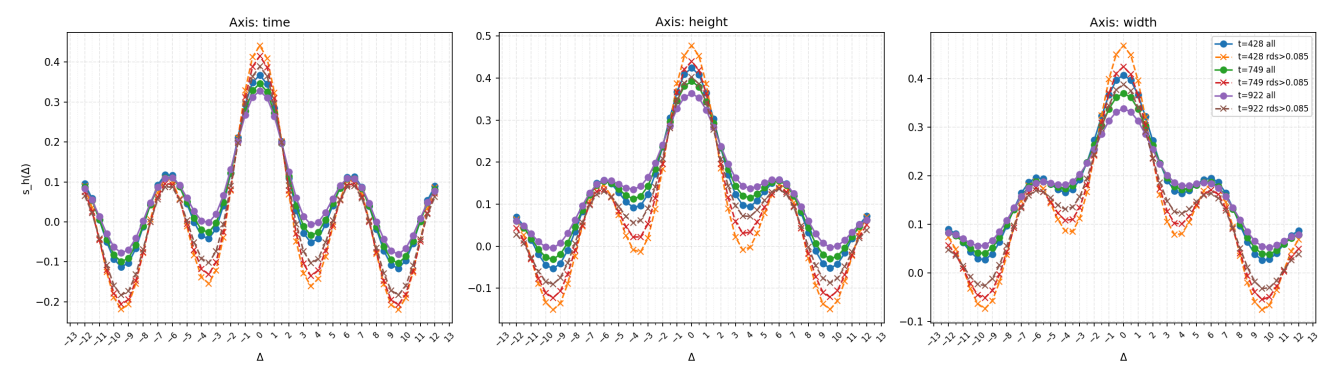


Figure 3. Attention Scores vs. RoPE relative distance Δ . Mean normalized scores $\kappa(\Delta)$ on Wan model [109] across diffusion steps $t \in \{428,749,922\}$. For each axis (time, height, width), curves are averaged over all attention heads and over RoPE-dominant heads, where RoPE dominance is defined by a head-level RoPE-dominance score (rds); heads with rds > 0.085 are classified as RoPE-dominant. The relative distance Δ denotes token offsets along the corresponding axis. We observe (i) strong periodicity with a sharp global maximum near $\Delta \approx 0$, (ii) amplification in RoPE-dominant heads, and (iii) stability across timesteps, suggesting a pretrained phase prior.

time, height, and width axes, and additionally analyze *RoPE-dominant* heads selected by the RoPE-dominance score (*rds*) following [15].

Empirical behavior. As shown in Fig. 3, we observe three consistent phenomena across layers and timesteps:

- 1. Sharp peak and steep near-zero decay. $\kappa(\Delta)$ attains its global maximum near $\Delta \approx 0$, with a pronounced drop within the first 2–3 offsets.
- 2. **Strong periodic structure.** The curves exhibit clear oscillations in Δ , reflecting multi-frequency phase responses originating from the RoPE basis.
- 3. **Amplification in RoPE-dominant heads, stable across timesteps.** Heads with higher *rds* show larger amplitudes and steeper slopes, and this structure persists across early, middle, and late diffusion steps. The effect therefore reflects a *pretrained phase prior*, not a transient denoising artifact.

These properties jointly explain why both interpolation schemes in Sec. 3.2 fail. Because the learned phase kernels peak extremely sharply near $\Delta=0$ and vary rapidly, even small distortions in the offset—such as those introduced when LR and HR grids are forced into a single index space—produce large, systematic deviations in the expected kernel response. These observations suggest that attention heads do not merely favor local proximity; instead, they implement *learned phase filters* whose responses depend intricately on the phase shift imposed by RoPE.

Interpreting the curves via kernel decomposition. In fact, using the relative form of RoPE (Eq. (3)), the attention score between a query–key pair averaging over content can be written as:

$$score(q, k, \Delta) = \sum_{i} C_i(q, k) \cos(\omega_i \Delta + \phi_i), \quad (6)$$

where ω_i are fixed RoPE frequencies, and (C_i, ϕ_i) are content- and head-dependent coefficients (see proof in the

supplementary material).

Equation (6) shows that each head behaves like a *mixture of sinusoidal kernels* over Δ . High-frequency components (ω_i large) produce steep near-zero slopes and strong periodicity, exactly matching the empirical patterns above. Thus, the measured $\kappa(\Delta)$ is the head's learned *phase kernel*—a function governing how much the head amplifies or suppresses attention as a function of relative offset.

Importantly, the kernel in Eq. (6) assumes that Δ is measured using a *single* spatial stride. Mixed-resolution interpolation breaks this assumption: LR and HR grids map the same physical distance to different index increments, so any unified index space inevitably assigns inconsistent Δ values across regions. This geometric inconsistency is incompatible with the learned phase structure of the heads and explains the complementary failure modes observed in Sec. 3.2. Overall, the issue is not the choice of interpolation scheme but the lack of a uniform sampling rate for Δ . Stable mixed-resolution attention therefore requires all RoPE phases within a dot-product to be expressed on a coherent reference grid. We introduce such a mechanism next.

4. Method

The analysis in Sec. 3.3 shows that pretrained DiT attention heads implement sharply tuned, multi-frequency phase kernels whose responses are valid only when relative offsets Δ are sampled at a single, consistent spatial stride. Mixed-resolution interpolation violates this assumption: LR and HR tokens map the same physical distance to different index increments, causing incompatible phase samples to be fed into the same kernel. To restore stable attention, we follow a simple principle:

One attention, one scale: within every query–key–value dot product, all RoPE phases must be expressed on a single, coherent reference grid.

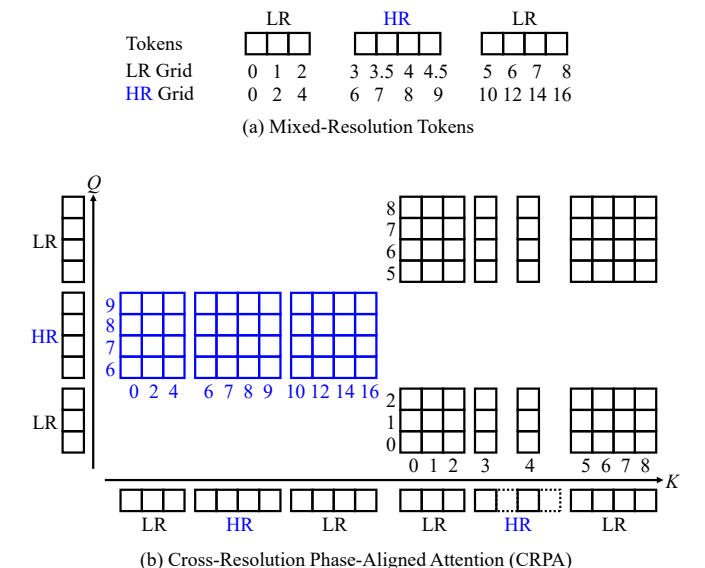


Figure 4. Cross-Resolution Phase-Aligned Attention (CRPA). For each attention call, RoPE indices of keys are rescaled onto the query grid so that equal physical distances yield identical phase increments, eliminating cross-rate aliasing and enabling stable mixed-resolution denoising with arbitrary LR/HR layouts.

We implement this requirement using *Cross-Resolution Phase-Aligned Attention (CRPA)*, a training-free mechanism that aligns RoPE index geometry across sampling rates. To further smooth content transitions between LR and HR regions, we introduce an additional Boundary Expandand-Replace module. Together, these components form a stable and efficient mixed-resolution denoising pipeline.

4.1. Cross-Resolution Phase-Aligned Attention

Let S_q and S_k denote the native grid spacings (LR/HR) of the query and key/value tokens, and define the scale ratio

$$\alpha_{k \to q} = \frac{S_q}{S_k}.$$

Before applying RoPE, we re-index every key/value position to the query's reference grid:

$$p_k^{(q)} \; = \; \alpha_{k \! \to \! q} \, p_k, \qquad \widetilde{q} \; = \; \mathcal{R}(p_q) \, q, \qquad \widetilde{k} \; = \; \mathcal{R}\!\!\left(p_k^{(q)}\right) k,$$

and compute the score

$$\langle \widetilde{q}, \widetilde{k} \rangle = \langle q, \mathcal{R}(\alpha_{k \to q} p_k - p_q) k \rangle,$$

which depends on a single relative offset $\Delta^{(q)} = \alpha_{k \to q} p_k - p_q$ measured in the query's units. In words: we never feed cross-rate phases into the same head; we always compare phases sampled on the query's scale.

As illustrated in Fig. 4:

• *High-res query*. If the query is HR (e.g., indices [6, 7, 8, 9] in the toy example), LR keys/values are lifted

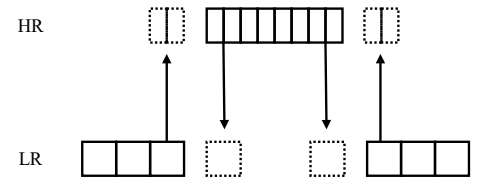


Figure 5. **Boundary Expand-and-Replace.** Around LR–HR boundaries, we dilate the masks and bidirectionally exchange upsampled and downsampled latent content within a narrow band, harmonizing textures while adding negligible overhead.

by index stretching before RoPE (e.g., LR [0,2,4] and [10,12,14,16] are evaluated at their HR-referenced positions). Content remains at LR fidelity; only the RoPE indices are lifted.

Low-res query. If the query is LR (e.g., [0, 1, 2] and [5, 6, 7, 8]), HR keys/values are subsampled to the LR grid both in content and in RoPE positions (e.g., compressing [6, 7, 8, 9] → [3, 4]) before the dot product.

CRPA is entirely training-free and drop-in: it modifies only the RoPE index map for each attention call so that equal physical distances yield identical phase increments. By expressing all Q/K positions on the query's stride, CRPA restores consistent phase sampling across resolutions and removes the aliasing and oversampling effects introduced by interpolation. Beyond correcting the failure mode, it remains compatible with any pretrained DiT; it stabilizes all heads and layers uniformly, supports arbitrary LR/HR layouts, irregular masks, and mixed spatiotemporal grids without redesign; and it incurs negligible computational overhead while remaining compatible with optimized attention kernels.

4.2. Extension: Boundary Expand-and-Replace

CRPA resolves the phase mismatch between resolutions, but small visual discontinuities may still appear near LR–HR boundaries (*e.g.*, slight density or texture shifts). We mitigate these with a lightweight, localized harmonization step that operates only in a narrow band around the boundaries (Fig. 5).

Given the LR and HR token masks, we first dilate each mask by $n_{\rm pad}$ (e.g., 2) tokens to form an overlapping boundary band. At each diffusion step t, with noisy latent x_t and current clean estimate x_0 , we perform a bidirectional content exchange within this band:

- $Low \rightarrow High$. Upsample the LR portion of x_0 using a learned latent upsampler, re-noise it to timestep t-1, and replace HR tokens in the band for the next denoising step.
- $High \rightarrow Low$. Downsample the HR portion of x_0 , re-noise it similarly, and replace the LR tokens in the band.

Because these tokens act only as attention context and not as final outputs, a small 25M resizer model is sufficient. This localized exchange reduces boundary artifacts without introducing global overhead.

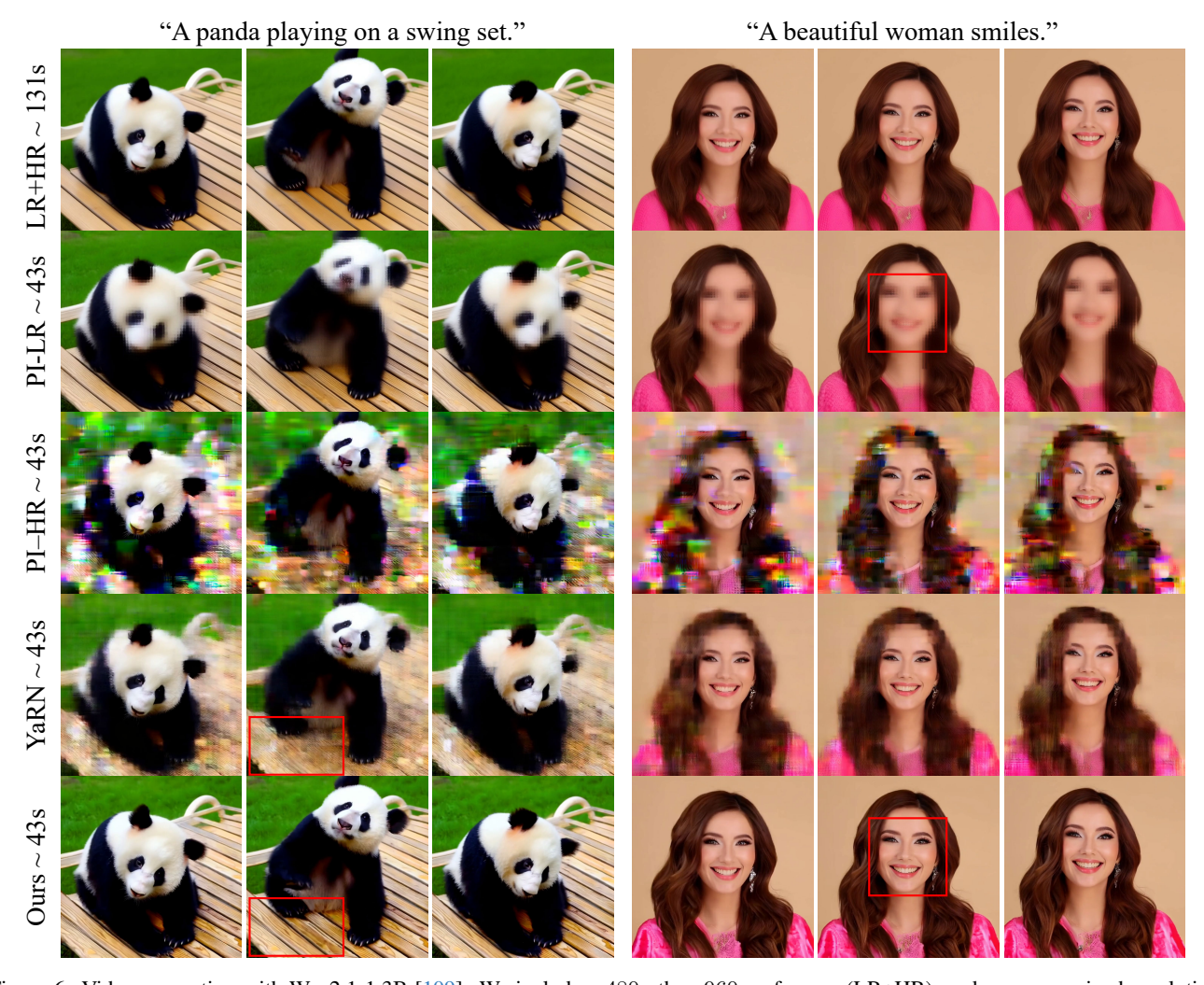


Figure 6. Video generation with Wan2.1-1.3B [109]. We include a 480p-then-960p reference (LR+HR), and compare mixed-resolution denoising using RoPE with linear interpolation [13] to low- or high-resolution grids (PI-LR/PI-HR), YaRN [79], and our method.

4.3. Use Case: Importance-Based Mixed-Resolution Denoising

CRPA makes mixed-resolution denoising stable in practice. Building on this capability, we assign high resolution selectively to salient regions (e.g., faces, motion boundaries, fine-detail areas) identified by a lightweight detector. This pipeline can operate in either two or three stages, depending on the desired trade-off between speed and quality:

- 1. *Coarse*. We perform low-resolution denoising to quickly establish the overall structure and motion of the scene.
- 2. *Mixed-Resolution*. A lightweight saliency detector identifies regions of higher importance. For salient regions, we switch to high resolution, while keeping other areas at low resolution. The denoising is conducted using the proposed mixed-resolution techniques.
- 3. *Fine*. Optionally, the final few steps are refined at full resolution to enhance visual details.

This design achieves practical acceleration for video and image DiT models while maintaining high visual quality.

5. Experiments

5.1. Experimental Settings

Video DiT. We build on Wan 2.1 [109] as the base text-to-video model. We adopt a two-stage inference scheme: a coarse stage at 480p followed by a mixed-resolution stage that jointly processes 480p and 960p tokens. For mixed-resolution denoising, we compare several RoPE interpolation strategies, including linear position interpolation to the low-resolution grid (PI-LR) [13] or the high-resolution grid (PI-HR), NTK-aware interpolation (NTK) [78], a hybrid of linear and NTK-aware interpolation (PI+NTK), and YaRN [79]. We also include high-resolution-only baselines that perform denoising entirely at 960p, as well as a two-stage 480p-then-960p schedule that serves as an upper-



Figure 7. Mixed-resolution image generation results on FLUX [53] comparing RoPE with linear interpolation [13] to low and high resolution grids (PI-LR/PI-HR) against our method.

Method		DOVER			VBench				
Method	Aes.	Tech.	All	Qual.	Sem.	Tot.	Time		
HR	99.83	10.43	79.12	0.801	0.623	0.766	172 s		
LR+HR	99.63	9.26	74.88	0.804	0.593	0.762	131 s		
PI-LR [13]	98.10	8.01	63.39	0.759	0.549	0.717			
PI-HR [13]	86.52	4.94	35.04	0.704	0.494	0.661			
NTK [78]	92.76	5.89	44.52	0.718	0.529	0.680	43 s		
PI+NTK	98.07	7.71	62.67	0.756	0.561	0.717			
YARN [79]	<u>98.56</u>	<u>8.96</u>	66.38	<u>0.764</u>	0.567	0.725			
Ours	99.63	10.01	75.34	0.808	0.622	0.770	43 s		

Table 1. Quantitative comparison of RoPE interpolation methods for mixed-resolution denosing on Wan2.1-1.3B [109] using DOVER [117] (Aesthetic, Technical, Overall) and VBench [39] (Quality, Semantics, Total); higher is better except for generation time. We include an HR baseline that denoise at 960p and a two-stage $480p \rightarrow 960p$ schedule (LR+HR) as a reference.

Method	FID↓	CLIP-IQA↑	MUSIQ↑	CLIP↑	Time↓
HR	31.50	0.640	71.48	31.03	4.1 s
PI-LR [13]	41.45	0.425	55.79	31.24	
PI-HR [13]	49.84	0.295	65.68	30.74	
NTK [78]	42.43	0.341	<u>65.80</u>	31.07	2.8 s
YARN [79]	<u>33.83</u>	0.434	65.64	31.27	
Ours	32.04	0.563	68.88	31.18	

Table 2. Quantitative comparison of RoPE interpolation methods for mixed-resolution denosing on Flux.1-dev [53]. We include an HR baseline that denoises at high resolution as a reference.

bound reference for mixed-resolution inference.

Image DiT. For image generation, we use Flux.1-dev [53] as the base text-to-image model. We set the coarse resolu-



Figure 8. Three-stage generation comparison on Flux [53], evaluating 18- and 9-step denosing with RALU [42] and our method, using FLUX (50 high-resolution steps) as the reference.

tion to 512 and the fine resolution to 1024, and evaluate a two-stage inference scheme (coarse and mixed-resolution). In addition, we also study a three-stage setting (coarse, mixed, and fine).

Implementation Details. For video generation, we use 50

Method	FID↓	CLIP-IQA↑	MUSIQ↑	CLIP↑	Time↓
FLUX-50	32.67	0.647	71.90	30.82	11.5 s
RALU-18	32.91	0.556	69.87	31.03	2.7 s
Ours-18	32.45	0.601	72.22	31.17	2.8 s
RALU-9	40.49	0.540	60.03	30.77	1.7 s
Ours-9	32.08	0.575	67.35	31.25	1.7 s

Table 3. Quantitative comparison of three-stage image-generation schedules (low—mixed—high resolution) on Flux.1-dev [53], under 18- and 9-step settings using RALU [42] and our method, with FLUX (50 high-res steps) as the reference.

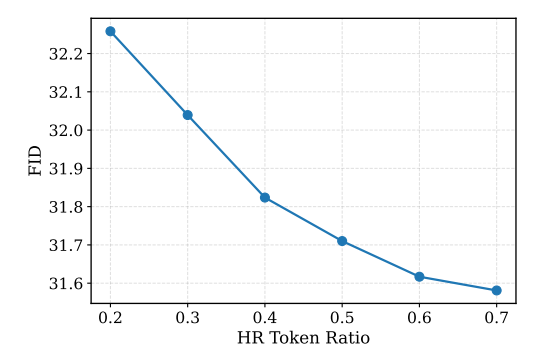


Figure 9. Quality-cost trade-off of the proposed mixed-resolution strategy on FLUX [53], illustrating how image quality changes with varying high-resolution token ratios.

denoising steps in total: 15 steps at 480p and 35 mixedresolution steps, with a high-resolution token ratio of 15% during the mixed-resolution stage. For image generation in the two-stage setting, we use 18 denoising steps: 7 steps at 512 and 11 mixed-resolution steps, with a 30% highresolution token ratio. In the three-stage image setting, we adopt a RALU-like schedule [42] with a small number of steps at the final high-resolution stage and apply noise rescheduling accordingly. To select salient regions, we first use tiny VAE decoders [5] to reconstruct coarse images or videos following the low-resolution denoising stage, and then apply DeepGazeIIE [60] to detect these regions. For video evaluation, we use VBench [39] and DOVER [117] as benchmarks and also report generation latency. For images, we report FID [37], MUSIQ [47], and CLIP-IQA [110] for image quality assessment, CLIP score [86] for prompt alignment, and generation latency.

5.2. Results

Video DiT. As shown in Tab. 1 and Fig. 6, our mixed-resolution RoPE scheme significantly outperforms existing RoPE interpolation baselines for mixed-resolution denoising. Compared to linear position interpolation [13] (to either low- or high-resolution grids), NTK-aware interpolation [78], their hybrids, and YaRN [79], our method achieves consistently better VBench and DOVER scores



(a) w/o Expand-and-Replace (b) w/ Expand-and-Replace

Figure 10. Ablation of the Boundary Expand-and-Replace procedure, where enabling it yields smoother and more coherent content across resolution boundaries.

at similar latency. In addition, our method attains quality that is close to the high-resolution-only 960p baseline and the 480p-then-960p upper-bound reference, while remaining substantially faster than these full high-resolution variants.

Image DiT. The image results, summarized in Tab. 2 and Fig. 7, show that our mixed-resolution RoPE method clearly outperforms all RoPE interpolation baselines. In the three-stage (coarse-mixed-fine) setting (Fig. 8 and Tab. 3), our method also surpasses RALU [42], even though RALU already employs a mixed-resolution stage; we attribute this improvement to replacing the naive linear positional interpolation used in RALU with our strategy. As shown in Fig. 9, the quality-cost curve indicates that we obtain strong performance even with a small high-resolution token ratio: quality improves rapidly in the low-ratio regime and then saturates as the high-resolution ratio increases, highlighting the effectiveness and efficiency of our design.

5.3. Ablation Study

In Fig. 10, we present an ablation study on the effectiveness of our Boundary Expand-and-Replace procedure. Without this component, the generated outputs appear plausible but exhibit subtle content discrepancies near the boundary when the underlying token resolution changes. In contrast, enabling the procedure produces results that are noticeably smoother and more coherent across the boundary.

6. Conclusion

We show that standard RoPE interpolation fundamentally breaks mixed-resolution denoising in DiTs: the model is forced to compare phases sampled at incompatible spatial rates, producing cross-rate aliasing and chaotic attention. To eliminate this failure mode, we introduce Cross-Resolution Phase-Aligned Attention, which enforces a strict principle—one attention, one scale—and adds a lightweight Boundary Expand-and-Replace step to smooth resolution transitions. This design is training-free, drop-in, and compatible with any pretrained DiT, giving reliable, high-fidelity image and video generation at reduced cost while preserving model architecture and speed.

7. Acknowledgments

We are grateful to Meher Gitika Karumuri, Brandon Smith, Amogh Gupta, and Vidya Narayanan for their insightful comments and valuable discussions. This work was supported in part by NSF grants IIS-2123920 and IIS-2212046.

References

- [1] Shubham Agarwal, Subrata Mitra, Sarthak Chakraborty, Srikrishna Karanam, Koyel Mukherjee, and Shiv Kumar Saini. Approximate caching for efficiently serving {Textto-Image} diffusion models. In 21st USENIX Symposium on Networked Systems Design and Implementation (NSDI 24), pages 1173–1189, 2024. 2
- [2] Jinze Bai, Shuai Bai, Yunfei Chu, Zeyu Cui, Kai Dang, Xiaodong Deng, Yang Fan, Wenbin Ge, Yu Han, Fei Huang, et al. Qwen technical report. arXiv preprint arXiv:2309.16609, 2023. 1
- [3] Federico Barbero, Alex Vitvitskyi, Christos Perivolaropoulos, Razvan Pascanu, and Petar Veličković. Round and round we go! what makes rotary positional encodings useful? arXiv preprint arXiv:2410.06205, 2024. 1
- [4] Sidney Black, Stella Biderman, Eric Hallahan, Quentin Anthony, Leo Gao, Laurence Golding, Horace He, Connor Leahy, Kyle McDonell, Jason Phang, et al. Gpt-neox-20b: An open-source autoregressive language model. In Proceedings of BigScience Episode# 5-Workshop on Challenges & Perspectives in Creating Large Language Models, pages 95–136, 2022. 1
- [5] Ollin Boer Bohan. Taehv: Tiny autoencoder for hunyuan video. https://github.com/madebyollin/ taehv, 2025. 8, 17, 18
- [6] Daniel Bolya and Judy Hoffman. Token merging for fast stable diffusion. In *Proceedings of the IEEE/CVF conference on computer vision and pattern recognition*, pages 4599–4603, 2023. 2
- [7] Thibault Castells, Hyoung-Kyu Song, Bo-Kyeong Kim, and Shinkook Choi. Ld-pruner: Efficient pruning of latent diffusion models using task-agnostic insights. In Proceedings of the IEEE/CVF Conference on Computer Vision and Pattern Recognition, pages 821–830, 2024. 2
- [8] Shuning Chang, WANG Pichao, Jiasheng Tang, Fan Wang, and Yi Yang. Sparsedit: Token sparsification for efficient diffusion transformer. In *The Thirty-ninth Annual Confer*ence on Neural Information Processing Systems, 2025. 2
- [9] Junsong Chen, Jincheng Yu, Chongjian Ge, Lewei Yao, Enze Xie, Yue Wu, Zhongdao Wang, James Kwok, Ping Luo, Huchuan Lu, and Zhenguo Li. Pixart-α: Fast training of diffusion transformer for photorealistic text-to-image synthesis, 2023. 2
- [10] Lei Chen, Yuan Meng, Chen Tang, Xinzhu Ma, Jingyan Jiang, Xin Wang, Zhi Wang, and Wenwu Zhu. Q-dit: Accurate post-training quantization for diffusion transformers. In *Proceedings of the Computer Vision and Pattern Recognition Conference*, pages 28306–28315, 2025. 2

- [11] Pengtao Chen, Mingzhu Shen, Peng Ye, Jianjian Cao, Chongjun Tu, Christos-Savvas Bouganis, Yiren Zhao, and Tao Chen. A training-free acceleration method tailored for diffusion transformers. arXiv preprint arXiv:2406.01125, 2024. 2
- [12] Pengtao Chen, Xianfang Zeng, Maosen Zhao, Peng Ye, Mingzhu Shen, Wei Cheng, Gang Yu, and Tao Chen. Sparse-vdit: Unleashing the power of sparse attention to accelerate video diffusion transformers. arXiv preprint arXiv:2506.03065, 2025. 2
- [13] Shouyuan Chen, Sherman Wong, Liangjian Chen, and Yuandong Tian. Extending context window of large language models via positional interpolation. *arXiv preprint arXiv:2306.15595*, 2023. 1, 2, 3, 6, 7, 8, 19
- [14] Xinwang Chen, Ning Liu, Yichen Zhu, Feifei Feng, and Jian Tang. Edt: An efficient diffusion transformer framework inspired by human-like sketching. Advances in Neural Information Processing Systems, 37:134075–134106, 2024. 2
- [15] Yiting Chen and Junchi Yan. What rotary position embedding can tell us: Identifying query and key weights corresponding to basic syntactic or high-level semantic information. *Advances in Neural Information Processing Systems*, 37:54507–54528, 2024. 2, 4, 19
- [16] Aakanksha Chowdhery, Sharan Narang, Jacob Devlin, Maarten Bosma, Gaurav Mishra, Adam Roberts, Paul Barham, Hyung Won Chung, Charles Sutton, Sebastian Gehrmann, et al. Palm: Scaling language modeling with pathways. *Journal of Machine Learning Research*, 24(240): 1–113, 2023. 1
- [17] Marcella Cornia, Lorenzo Baraldi, Giuseppe Serra, and Rita Cucchiara. A deep multi-level network for saliency prediction. In 2016 23rd International Conference on Pattern Recognition (ICPR), pages 3488–3493. IEEE, 2016.
- [18] Marcella Cornia, Lorenzo Baraldi, Giuseppe Serra, and Rita Cucchiara. Predicting human eye fixations via an lstmbased saliency attentive model. *IEEE Transactions on Im*age Processing, 27(10):5142–5154, 2018. 20
- [19] Katherine Crowson, Stefan Andreas Baumann, Alex Birch, Tanishq Mathew Abraham, Daniel Z Kaplan, and Enrico Shippole. Scalable high-resolution pixel-space image synthesis with hourglass diffusion transformers. In Forty-first International Conference on Machine Learning, 2024. 1
- [20] Juncan Deng, Shuaiting Li, Zeyu Wang, Hong Gu, Kedong Xu, and Kejie Huang. Vq4dit: Efficient post-training vector quantization for diffusion transformers. In *Proceedings* of the AAAI Conference on Artificial Intelligence, pages 16226–16234, 2025. 2
- [21] Yiran Ding, Li Lyna Zhang, Chengruidong Zhang, Yuanyuan Xu, Ning Shang, Jiahang Xu, Fan Yang, and Mao Yang. Longrope: Extending llm context window beyond 2 million tokens. *arXiv preprint arXiv:2402.13753*, 2024. 2
- [22] Zheng Ding, Mengqi Zhang, Jiajun Wu, and Zhuowen Tu. Patched denoising diffusion models for high-resolution image synthesis. In *The Twelfth International Conference on Learning Representations*, 2024. 2

- [23] Alexey Dosovitskiy. An image is worth 16x16 words: Transformers for image recognition at scale. arXiv preprint arXiv:2010.11929, 2020. 20
- [24] Zhenbang Du, Yonggan Fu, Lifu Wang, Jiayi Qian, Xiao Luo, and Yingyan Celine Lin. Fewer denoising steps or cheaper per-step inference: Towards compute-optimal diffusion model deployment. In *Proceedings of the IEEE/CVF International Conference on Computer Vision*, pages 3001–3010, 2025.
- [25] Abhimanyu Dubey, Abhinav Jauhri, Abhinav Pandey, Abhishek Kadian, Ahmad Al-Dahle, Aiesha Letman, Akhil Mathur, Alan Schelten, Amy Yang, Angela Fan, et al. The llama 3 herd of models. arXiv e-prints, pages arXiv–2407, 2024. 1
- [26] Patrick Esser, Sumith Kulal, Andreas Blattmann, Rahim Entezari, Jonas Müller, Harry Saini, Yam Levi, Dominik Lorenz, Axel Sauer, Frederic Boesel, et al. Scaling rectified flow transformers for high-resolution image synthesis. In Forty-first international conference on machine learning, 2024. 2
- [27] Gongfan Fang, Xinyin Ma, and Xinchao Wang. Structural pruning for diffusion models. In Advances in Neural Information Processing Systems, 2023. 2
- [28] Gongfan Fang, Kunjun Li, Xinyin Ma, and Xinchao Wang. Tinyfusion: Diffusion transformers learned shallow. In Proceedings of the Computer Vision and Pattern Recognition Conference, pages 18144–18154, 2025. 2
- [29] Zhengcong Fei, Di Qiu, Debang Li, Changqian Yu, and Mingyuan Fan. Video diffusion transformers are in-context learners. arXiv preprint arXiv:2412.10783, 2024. 2
- [30] Weilun Feng, Chuanguang Yang, Zhulin An, Libo Huang, Boyu Diao, Fei Wang, and Yongjun Xu. Relational diffusion distillation for efficient image generation. In *Proceedings of the 32nd ACM international conference on multimedia*, pages 205–213, 2024. 2
- [31] Yifei Feng, Mingxin Yang, Shuhui Yang, Sheng Zhang, Jiaao Yu, Zibo Zhao, Yuhong Liu, Jie Jiang, and Chunchao Guo. Romantex: Decoupling 3d-aware rotary positional embedded multi-attention network for texture synthesis. In *Proceedings of the IEEE/CVF International Conference on Computer Vision*, pages 17203–17213, 2025.
- [32] Alireza Ganjdanesh, Reza Shirkavand, Shangqian Gao, and Heng Huang. Not all prompts are made equal: Prompt-based pruning of text-to-image diffusion models. *arXiv* preprint arXiv:2406.12042, 2024. 2
- [33] Daya Guo, Dejian Yang, Haowei Zhang, Junxiao Song, Ruoyu Zhang, Runxin Xu, Qihao Zhu, Shirong Ma, Peiyi Wang, Xiao Bi, et al. Deepseek-r1: Incentivizing reasoning capability in Ilms via reinforcement learning. *arXiv* preprint arXiv:2501.12948, 2025. 1
- [34] Yoav HaCohen, Nisan Chiprut, Benny Brazowski, Daniel Shalem, Dudu Moshe, Eitan Richardson, Eran Levin, Guy Shiran, Nir Zabari, Ori Gordon, et al. Ltx-video: Realtime video latent diffusion. *arXiv preprint arXiv:2501.00103*, 2024. 1, 2
- [35] Jonathan Harel, Christof Koch, and Pietro Perona. Graphbased visual saliency. In *Advances in Neural Information Processing Systems*. MIT Press, 2006. 20

- [36] Byeongho Heo, Song Park, Dongyoon Han, and Sangdoo Yun. Rotary position embedding for vision transformer. In European Conference on Computer Vision, pages 289–305. Springer, 2024. 1, 2
- [37] Martin Heusel, Hubert Ramsauer, Thomas Unterthiner, Bernhard Nessler, and Sepp Hochreiter. Gans trained by a two time-scale update rule converge to a local nash equilibrium. Advances in neural information processing systems, 30, 2017. 8, 18
- [38] Jonathan Ho, Chitwan Saharia, William Chan, David J Fleet, Mohammad Norouzi, and Tim Salimans. Cascaded diffusion models for high fidelity image generation. *Journal of Machine Learning Research*, 23(47):1–33, 2022. 2
- [39] Ziqi Huang, Yinan He, Jiashuo Yu, Fan Zhang, Chenyang Si, Yuming Jiang, Yuanhan Zhang, Tianxing Wu, Qingyang Jin, Nattapol Chanpaisit, et al. Vbench: Comprehensive benchmark suite for video generative models. In Proceedings of the IEEE/CVF Conference on Computer Vision and Pattern Recognition, pages 21807–21818, 2024. 7, 8, 18, 19
- [40] Laurent Itti, Christof Koch, and Ernst Niebur. A model of saliency-based visual attention for rapid scene analysis. *IEEE Transactions on pattern analysis and machine intelligence*, 20(11):1254–1259, 2002. 20
- [41] Jinho Jeong, Sangmin Han, Jinwoo Kim, and Seon Joo Kim. Latent space super-resolution for higher-resolution image generation with diffusion models. In *Proceedings of* the Computer Vision and Pattern Recognition Conference, pages 2355–2365, 2025. 2
- [42] Wongi Jeong, Kyungryeol Lee, Hoigi Seo, and Se Young Chun. Upsample what matters: Region-adaptive latent sampling for accelerated diffusion transformers. *arXiv* preprint arXiv:2507.08422, 2025. 1, 2, 7, 8, 17, 18
- [43] Sen Jia and Neil DB Bruce. Eml-net: An expandable multilayer network for saliency prediction. *Image and vision computing*, 95:103887, 2020. 20
- [44] Ming Jiang, Shengsheng Huang, Juanyong Duan, and Qi Zhao. Salicon: Saliency in context. In *Proceedings of the IEEE conference on computer vision and pattern recognition*, pages 1072–1080, 2015. 20
- [45] Yang Jin, Zhicheng Sun, Ningyuan Li, Kun Xu, Hao Jiang, Nan Zhuang, Quzhe Huang, Yang Song, Yadong Mu, and Zhouchen Lin. Pyramidal flow matching for efficient video generative modeling. arXiv preprint arXiv:2410.05954, 2024. 2
- [46] Kumara Kahatapitiya, Haozhe Liu, Sen He, Ding Liu, Menglin Jia, Chenyang Zhang, Michael S Ryoo, and Tian Xie. Adaptive caching for faster video generation with diffusion transformers. In *Proceedings of the IEEE/CVF In*ternational Conference on Computer Vision, pages 15240– 15252, 2025. 2
- [47] Junjie Ke, Qifei Wang, Yilin Wang, Peyman Milanfar, and Feng Yang. Musiq: Multi-scale image quality transformer. In *Proceedings of the IEEE/CVF international conference* on computer vision, pages 5148–5157, 2021. 8, 17, 18
- [48] Wolf Kienzle, Felix A Wichmann, Matthias Franz, and Bernhard Schölkopf. A nonparametric approach to bottom-

- up visual saliency. Advances in neural information processing systems, 19, 2006. 20
- [49] Younghyun Kim, Geunmin Hwang, Junyu Zhang, and Eunbyung Park. Diffusehigh: Training-free progressive high-resolution image synthesis through structure guidance. In *Proceedings of the AAAI conference on artificial intelligence*, pages 4338–4346, 2025. 20
- [50] Alex Krizhevsky, Ilya Sutskever, and Geoffrey E Hinton. Imagenet classification with deep convolutional neural networks. Advances in neural information processing systems, 25, 2012. 20
- [51] Srinivas SS Kruthiventi, Kumar Ayush, and R Venkatesh Babu. Deepfix: A fully convolutional neural network for predicting human eye fixations. *IEEE Transactions on Im*age Processing, 26(9):4446–4456, 2017. 20
- [52] Matthias Kümmerer, Lucas Theis, and Matthias Bethge. Deep gaze i: Boosting saliency prediction with feature maps trained on imagenet. *arXiv preprint arXiv:1411.1045*, 2014. 20
- [53] Black Forest Labs, Stephen Batifol, Andreas Blattmann, Frederic Boesel, Saksham Consul, Cyril Diagne, Tim Dockhorn, Jack English, Zion English, Patrick Esser, Sumith Kulal, Kyle Lacey, Yam Levi, Cheng Li, Dominik Lorenz, Jonas Müller, Dustin Podell, Robin Rombach, Harry Saini, Axel Sauer, and Luke Smith. Flux.1 kontext: Flow matching for in-context image generation and editing in latent space, 2025. 1, 2, 7, 8, 16, 17, 18, 19, 22
- [54] Hao Li, Shamit Lal, Zhiheng Li, Yusheng Xie, Ying Wang, Yang Zou, Orchid Majumder, R Manmatha, Zhuowen Tu, Stefano Ermon, et al. Efficient scaling of diffusion transformers for text-to-image generation. arXiv preprint arXiv:2412.12391, 2024. 2
- [55] Muyang Li, Yujun Lin, Zhekai Zhang, Tianle Cai, Xiuyu Li, Junxian Guo, Enze Xie, Chenlin Meng, Jun-Yan Zhu, and Song Han. Svdquant: Absorbing outliers by low-rank components for 4-bit diffusion models. arXiv preprint arXiv:2411.05007, 2024. 2
- [56] Yanyu Li, Huan Wang, Qing Jin, Ju Hu, Pavlo Chemerys, Yun Fu, Yanzhi Wang, Sergey Tulyakov, and Jian Ren. Snapfusion: Text-to-image diffusion model on mobile devices within two seconds. *Advances in Neural Information Processing Systems*, 36:20662–20678, 2023. 2
- [57] Zhimin Li, Jianwei Zhang, Qin Lin, Jiangfeng Xiong, Yanxin Long, Xinchi Deng, Yingfang Zhang, Xingchao Liu, Minbin Huang, Zedong Xiao, et al. Hunyuandit: A powerful multi-resolution diffusion transformer with fine-grained chinese understanding. arXiv preprint arXiv:2405.08748, 2024. 2
- [58] Tsung-Yi Lin, Michael Maire, Serge Belongie, James Hays, Pietro Perona, Deva Ramanan, Piotr Dollár, and C Lawrence Zitnick. Microsoft coco: Common objects in context. In Computer Vision–ECCV 2014: 13th European Conference, Zurich, Switzerland, September 6-12, 2014, Proceedings, Part V 13, pages 740–755. Springer, 2014. 18
- [59] Akis Linardos, Matthias Kümmerer, Ori Press, and Matthias Bethge. Deepgaze iie: Calibrated prediction in and out-of-domain for state-of-the-art saliency modeling.

- In Proceedings of the IEEE/CVF International Conference on Computer Vision, pages 12919–12928, 2021. 20
- [60] Akis Linardos, Matthias Kümmerer, Ori Press, and Matthias Bethge. Deepgaze iie: Calibrated prediction in and out-of-domain for state-of-the-art saliency modeling. In Proceedings of the IEEE/CVF International Conference on Computer Vision, pages 12919–12928, 2021. 8, 17, 18
- [61] Feng Liu, Shiwei Zhang, Xiaofeng Wang, Yujie Wei, Haonan Qiu, Yuzhong Zhao, Yingya Zhang, Qixiang Ye, and Fang Wan. Timestep embedding tells: It's time to cache for video diffusion model. In *Proceedings of the Computer Vision and Pattern Recognition Conference*, pages 7353–7363, 2025. 2, 17
- [62] Nian Liu and Junwei Han. A deep spatial contextual longterm recurrent convolutional network for saliency detection. *IEEE Transactions on Image Processing*, 27(7):3264– 3274, 2018. 20
- [63] Ziming Liu, Yifan Yang, Chengruidong Zhang, Yiqi Zhang, Lili Qiu, Yang You, and Yuqing Yang. Region-adaptive sampling for diffusion transformers. arXiv preprint arXiv:2502.10389, 2025. 2
- [64] Jianxun Lou, Hanhe Lin, David Marshall, Dietmar Saupe, and Hantao Liu. Transalnet: Towards perceptually relevant visual saliency prediction. *Neurocomputing*, 494:455–467, 2022. 20
- [65] Jinming Lou, Wenyang Luo, Yufan Liu, Bing Li, Xinmiao Ding, Weiming Hu, Jiajiong Cao, Yuming Li, and Chenguang Ma. Token caching for diffusion transformer acceleration. arXiv preprint arXiv:2409.18523, 2024. 2
- [66] Cheng Lu, Yuhao Zhou, Fan Bao, Jianfei Chen, Chongxuan Li, and Jun Zhu. Dpm-solver: A fast ode solver for diffusion probabilistic model sampling in around 10 steps. Advances in neural information processing systems, 35:5775– 5787, 2022. 2
- [67] Cheng Lu, Yuhao Zhou, Fan Bao, Jianfei Chen, Chongxuan Li, and Jun Zhu. Dpm-solver++: Fast solver for guided sampling of diffusion probabilistic models. *Machine Intelligence Research*, pages 1–22, 2025. 2
- [68] Zeyu Lu, Zidong Wang, Di Huang, Chengyue Wu, Xihui Liu, Wanli Ouyang, and Lei Bai. Fit: Flexible vision transformer for diffusion model. arXiv preprint arXiv:2402.12376, 2024. 1, 2
- [69] Simian Luo, Yiqin Tan, Longbo Huang, Jian Li, and Hang Zhao. Latent consistency models: Synthesizing highresolution images with few-step inference. arXiv preprint arXiv:2310.04378, 2023. 2
- [70] Zhengyao Lv, Chenyang Si, Junhao Song, Zhenyu Yang, Yu Qiao, Ziwei Liu, and Kwan-Yee K Wong. Fastercache: Training-free video diffusion model acceleration with high quality. arXiv preprint arXiv:2410.19355, 2024. 2
- [71] Cheng Ma, Haowen Sun, Yongming Rao, Jie Zhou, and Jiwen Lu. Video saliency forecasting transformer. *IEEE transactions on circuits and systems for video technology*, 32(10):6850–6862, 2022. 20
- [72] Xinyin Ma, Gongfan Fang, Michael Bi Mi, and Xinchao Wang. Learning-to-cache: Accelerating diffusion transformer via layer caching. Advances in Neural Information Processing Systems, 37:133282–133304, 2024. 2

- [73] Xinyin Ma, Gongfan Fang, and Xinchao Wang. Deepcache: Accelerating diffusion models for free. In *Proceedings of the IEEE/CVF conference on computer vision and pattern recognition*, pages 15762–15772, 2024. 2
- [74] Xin Ma, Yaohui Wang, Gengyun Jia, Xinyuan Chen, Zi-wei Liu, Yuan-Fang Li, Cunjian Chen, and Yu Qiao. Latte: Latent diffusion transformer for video generation. arXiv preprint arXiv:2401.03048, 2024. 2
- [75] Zehong Ma, Longhui Wei, Feng Wang, Shiliang Zhang, and Qi Tian. Magcache: Fast video generation with magnitudeaware cache. arXiv preprint arXiv:2506.09045, 2025. 17
- [76] Sophie Ostmeier, Brian Axelrod, Michael E Moseley, Akshay Chaudhari, and Curtis Langlotz. Liere: Generalizing rotary position encodings. *arXiv preprint* arXiv:2406.10322, 2(4), 2024. 2
- [77] William Peebles and Saining Xie. Scalable diffusion models with transformers. In *Proceedings of the IEEE/CVF international conference on computer vision*, pages 4195–4205, 2023.
- [78] Bowen Peng and Jeffrey Quesnelle. Ntk-aware scaled rope allows llama models to have extended (8k+) context size without any fine-tuning and minimal perplexity degradation, 2023. 2, 6, 7, 8, 19
- [79] Bowen Peng, Jeffrey Quesnelle, Honglu Fan, and Enrico Shippole. Yarn: Efficient context window extension of large language models. *arXiv preprint arXiv:2309.00071*, 2023. 2, 6, 7, 8, 19, 20
- [80] Pablo Pernias, Dominic Rampas, Mats L Richter, Christopher J Pal, and Marc Aubreville. Würstchen: An efficient architecture for large-scale text-to-image diffusion models. arXiv preprint arXiv:2306.00637, 2023. 2
- [81] Dustin Podell, Zion English, Kyle Lacey, Andreas Blattmann, Tim Dockhorn, Jonas Müller, Joe Penna, and Robin Rombach. Sdxl: Improving latent diffusion models for high-resolution image synthesis. *arXiv preprint arXiv:2307.01952*, 2023. 2
- [82] Alexander Pondaven, Aliaksandr Siarohin, Sergey Tulyakov, Philip Torr, and Fabio Pizzati. Video motion transfer with diffusion transformers. In *Proceedings of the Computer Vision and Pattern Recognition Conference*, pages 22911–22921, 2025. 2
- [83] Ofir Press, Noah A Smith, and Mike Lewis. Train short, test long: Attention with linear biases enables input length extrapolation. arXiv preprint arXiv:2108.12409, 2021. 2
- [84] Haonan Qiu, Ning Yu, Ziqi Huang, Paul Debevec, and Ziwei Liu. Cinescale: Free lunch in high-resolution cinematic visual generation. *arXiv preprint arXiv:2508.15774*, 2025.
- [85] Haonan Qiu, Shiwei Zhang, Yujie Wei, Ruihang Chu, Hangjie Yuan, Xiang Wang, Yingya Zhang, and Ziwei Liu. Freescale: Unleashing the resolution of diffusion models via tuning-free scale fusion. In *Proceedings of the IEEE/CVF International Conference on Computer Vision*, pages 16893–16903, 2025. 20
- [86] Alec Radford, Jong Wook Kim, Chris Hallacy, Aditya Ramesh, Gabriel Goh, Sandhini Agarwal, Girish Sastry, Amanda Askell, Pamela Mishkin, Jack Clark, et al. Learn-

- ing transferable visual models from natural language supervision. In *International conference on machine learning*, pages 8748–8763. PmLR, 2021. 8, 18
- [87] Nikhila Ravi, Valentin Gabeur, Yuan-Ting Hu, Ronghang Hu, Chaitanya Ryali, Tengyu Ma, Haitham Khedr, Roman Rädle, Chloe Rolland, Laura Gustafson, et al. Sam 2: Segment anything in images and videos. arXiv preprint arXiv:2408.00714, 2024. 1
- [88] Robin Rombach, Andreas Blattmann, Dominik Lorenz, Patrick Esser, and Björn Ommer. High-resolution image synthesis with latent diffusion models. In *Proceedings of* the IEEE/CVF conference on computer vision and pattern recognition, pages 10684–10695, 2022. 2
- [89] Chitwan Saharia, William Chan, Saurabh Saxena, Lala Li, Jay Whang, Emily L Denton, Kamyar Ghasemipour, Raphael Gontijo Lopes, Burcu Karagol Ayan, Tim Salimans, et al. Photorealistic text-to-image diffusion models with deep language understanding. Advances in neural information processing systems, 35:36479–36494, 2022. 2
- [90] Tim Salimans and Jonathan Ho. Progressive distillation for fast sampling of diffusion models. arXiv preprint arXiv:2202.00512, 2022. 2
- [91] Hoigi Seo, Wongi Jeong, Jae-sun Seo, and Se Young Chun. Skrr: Skip and re-use text encoder layers for memory efficient text-to-image generation. arXiv preprint arXiv:2502.08690, 2025. 2
- [92] Yuzhang Shang, Zhihang Yuan, Bin Xie, Bingzhe Wu, and Yan Yan. Post-training quantization on diffusion models. In Proceedings of the IEEE/CVF conference on computer vision and pattern recognition, pages 1972–1981, 2023.
- [93] Oriane Siméoni, Huy V Vo, Maximilian Seitzer, Federico Baldassarre, Maxime Oquab, Cijo Jose, Vasil Khalidov, Marc Szafraniec, Seungeun Yi, Michaël Ramamonjisoa, et al. Dinov3. arXiv preprint arXiv:2508.10104, 2025. 1
- [94] Karen Simonyan and Andrew Zisserman. Very deep convolutional networks for large-scale image recognition. arXiv preprint arXiv:1409.1556, 2014. 20
- [95] Jiaming Song, Chenlin Meng, and Stefano Ermon. Denoising diffusion implicit models. arXiv preprint arXiv:2010.02502, 2020. 2
- [96] Yang Song, Prafulla Dhariwal, Mark Chen, and Ilya Sutskever. Consistency models. arXiv preprint arXiv:2303.01469, 2023. 2
- [97] Jianlin Su, Murtadha Ahmed, Yu Lu, Shengfeng Pan, Wen Bo, and Yunfeng Liu. Roformer: Enhanced transformer with rotary position embedding. *Neurocomputing*, 568: 127063, 2024. 1, 2
- [98] Yutao Sun, Li Dong, Barun Patra, Shuming Ma, Shaohan Huang, Alon Benhaim, Vishrav Chaudhary, Xia Song, and Furu Wei. A length-extrapolatable transformer. In Proceedings of the 61st annual meeting of the association for computational linguistics (volume 1: long papers), pages 14590–14604, 2023. 2
- [99] Bingda Tang, Boyang Zheng, Sayak Paul, and Saining Xie. Exploring the deep fusion of large language models and diffusion transformers for text-to-image synthesis. In Proceedings of the Computer Vision and Pattern Recognition Conference, pages 28586–28595, 2025. 2

- [100] Gemma Team, Thomas Mesnard, Cassidy Hardin, Robert Dadashi, Surya Bhupatiraju, Shreya Pathak, Laurent Sifre, Morgane Rivière, Mihir Sanjay Kale, Juliette Love, et al. Gemma: Open models based on gemini research and technology. arXiv preprint arXiv:2403.08295, 2024. 1
- [101] InternLM Team. Internlm: A multilingual language model with progressively enhanced capabilities, 2023. 1
- [102] Jiayan Teng, Wendi Zheng, Ming Ding, Wenyi Hong, Jian-qiao Wangni, Zhuoyi Yang, and Jie Tang. Relay diffusion: Unifying diffusion process across resolutions for image synthesis. arXiv preprint arXiv:2309.03350, 2023. 2
- [103] Yuchuan Tian, Zhijun Tu, Hanting Chen, Jie Hu, Chao Xu, and Yunhe Wang. U-dits: Downsample tokens in u-shaped diffusion transformers. Advances in Neural Information Processing Systems, 37:51994–52013, 2024. 1
- [104] Ye Tian, Xin Xia, Yuxi Ren, Shanchuan Lin, Xing Wang, Xuefeng Xiao, Yunhai Tong, Ling Yang, and Bin Cui. Training-free diffusion acceleration with bottleneck sampling. arXiv preprint arXiv:2503.18940, 2025. 2, 17, 18
- [105] Hugo Touvron, Thibaut Lavril, Gautier Izacard, Xavier Martinet, Marie-Anne Lachaux, Timothée Lacroix, Baptiste Rozière, Naman Goyal, Eric Hambro, Faisal Azhar, et al. Llama: Open and efficient foundation language models. arXiv preprint arXiv:2302.13971, 2023. 1
- [106] Ashish Vaswani, Noam Shazeer, Niki Parmar, Jakob Uszkoreit, Llion Jones, Aidan N Gomez, Łukasz Kaiser, and Illia Polosukhin. Attention is all you need. Advances in neural information processing systems, 30, 2017. 1, 20
- [107] Tobias Vontobel, Seyedmorteza Sadat, Farnood Salehi, and Romann M Weber. Hiwave: Training-free high-resolution image generation via wavelet-based diffusion sampling. arXiv preprint arXiv:2506.20452, 2025. 20
- [108] Ben Wan, Tianyi Zheng, Zhaoyu Chen, Yuxiao Wang, and Jia Wang. Pruning for sparse diffusion models based on gradient flow. In ICASSP 2025-2025 IEEE International Conference on Acoustics, Speech and Signal Processing (ICASSP), pages 1–5. IEEE, 2025. 2
- [109] Team Wan, Ang Wang, Baole Ai, Bin Wen, Chaojie Mao, Chen-Wei Xie, Di Chen, Feiwu Yu, Haiming Zhao, Jianxiao Yang, et al. Wan: Open and advanced large-scale video generative models. arXiv preprint arXiv:2503.20314, 2025. 1, 2, 4, 6, 7, 16, 17, 18, 19, 23
- [110] Jianyi Wang, Kelvin CK Chan, and Chen Change Loy. Exploring clip for assessing the look and feel of images. In AAAI, 2023. 8, 17, 18
- [111] Peng Wang, Shuai Bai, Sinan Tan, Shijie Wang, Zhihao Fan, Jinze Bai, Keqin Chen, Xuejing Liu, Jialin Wang, Wenbin Ge, et al. Qwen2-vl: Enhancing vision-language model's perception of the world at any resolution. *arXiv* preprint arXiv:2409.12191, 2024. 1
- [112] Wenguan Wang and Jianbing Shen. Deep visual attention prediction. *IEEE Transactions on Image Processing*, 27(5): 2368–2378, 2017. 20
- [113] Wenguan Wang, Jianbing Shen, Jianwen Xie, Ming-Ming Cheng, Haibin Ling, and Ali Borji. Revisiting video saliency prediction in the deep learning era. *IEEE transactions on pattern analysis and machine intelligence*, 43(1): 220–237, 2019. 20

- [114] Tianyi Wei, Yifan Zhou, Dongdong Chen, and Xingang Pan. Freeflux: Understanding and exploiting layer-specific roles in rope-based mmdit for versatile image editing. *arXiv* preprint arXiv:2503.16153, 2025. 1
- [115] Xilin Wei, Xiaoran Liu, Yuhang Zang, Xiaoyi Dong, Pan Zhang, Yuhang Cao, Jian Tong, Haodong Duan, Qipeng Guo, Jiaqi Wang, et al. Videorope: What makes for good video rotary position embedding? arXiv preprint arXiv:2502.05173, 2025.
- [116] Felix Wimbauer, Bichen Wu, Edgar Schoenfeld, Xiaoliang Dai, Ji Hou, Zijian He, Artsiom Sanakoyeu, Peizhao Zhang, Sam Tsai, Jonas Kohler, et al. Cache me if you can: Accelerating diffusion models through block caching. In *Proceedings of the IEEE/CVF Conference on Computer Vision and Pattern Recognition*, pages 6211–6220, 2024. 2
- [117] Haoning Wu, Erli Zhang, Liang Liao, Chaofeng Chen, Jingwen Hou Hou, Annan Wang, Wenxiu Sun Sun, Qiong Yan, and Weisi Lin. Exploring video quality assessment on user generated contents from aesthetic and technical perspectives. In *International Conference on Computer Vision* (ICCV), 2023. 7, 8, 18
- [118] Enze Xie, Junsong Chen, Yuyang Zhao, Jincheng Yu, Ligeng Zhu, Chengyue Wu, Yujun Lin, Zhekai Zhang, Muyang Li, Junyu Chen, et al. Sana 1.5: Efficient scaling of training-time and inference-time compute in linear diffusion transformer. arXiv preprint arXiv:2501.18427, 2025.
- [119] Zhucun Xue, Jiangning Zhang, Teng Hu, Haoyang He, Yinan Chen, Yuxuan Cai, Yabiao Wang, Chengjie Wang, Yong Liu, Xiangtai Li, et al. Ultravideo: High-quality uhd video dataset with comprehensive captions. arXiv preprint arXiv:2506.13691, 2025. 20
- [120] Zhuoyi Yang, Jiayan Teng, Wendi Zheng, Ming Ding, Shiyu Huang, Jiazheng Xu, Yuanming Yang, Wenyi Hong, Xiaohan Zhang, Guanyu Feng, et al. Cogvideox: Text-to-video diffusion models with an expert transformer. *arXiv* preprint arXiv:2408.06072, 2024. 1
- [121] Haoran You, Connelly Barnes, Yuqian Zhou, Yan Kang, Zhenbang Du, Wei Zhou, Lingzhi Zhang, Yotam Nitzan, Xiaoyang Liu, Zhe Lin, et al. Layer-and timestep-adaptive differentiable token compression ratios for efficient diffusion transformers. In *Proceedings of the Computer Vision* and Pattern Recognition Conference, pages 18072–18082, 2025. 2
- [122] Hao Yu, Tangyu Jiang, Shuning Jia, Shannan Yan, Shunning Liu, Haolong Qian, Guanghao Li, Shuting Dong, and Chun Yuan. Comrope: Scalable and robust rotary position embedding parameterized by trainable commuting angle matrices. In *Proceedings of the Computer Vision and Pattern Recognition Conference*, pages 4508–4517, 2025.
- [123] Aohan Zeng, Xiao Liu, Zhengxiao Du, Zihan Wang, Hanyu Lai, Ming Ding, Zhuoyi Yang, Yifan Xu, Wendi Zheng, Xiao Xia, et al. Glm-130b: An open bilingual pre-trained model. arXiv preprint arXiv:2210.02414, 2022. 1
- [124] Evelyn Zhang, Bang Xiao, Jiayi Tang, Qianli Ma, Chang Zou, Xuefei Ning, Xuming Hu, and Linfeng Zhang. Token

- pruning for caching better: 9 times acceleration on stable diffusion for free. *arXiv preprint arXiv:2501.00375*, 2024.
- [125] Evelyn Zhang, Jiayi Tang, Xuefei Ning, and Linfeng Zhang. Training-free and hardware-friendly acceleration for diffusion models via similarity-based token pruning. In Proceedings of the AAAI Conference on Artificial Intelligence, pages 9878–9886, 2025. 2
- [126] Linfeng Zhang and Kaisheng Ma. Accelerating diffusion models with one-to-many knowledge distillation. arXiv preprint arXiv:2410.04191, 2024. 2
- [127] Lingyun Zhang, Matthew H Tong, Tim K Marks, Honghao Shan, and Garrison W Cottrell. Sun: A bayesian framework for saliency using natural statistics. *Journal of vision*, 8(7): 32–32, 2008. 20
- [128] Yang Zhang, Er Jin, Yanfei Dong, Ashkan Khakzar, Philip Torr, Johannes Stegmaier, and Kenji Kawaguchi. Effortless efficiency: Low-cost pruning of diffusion models. arXiv preprint arXiv:2412.02852, 2024. 2
- [129] Min Zhao, Guande He, Yixiao Chen, Hongzhou Zhu, Chongxuan Li, and Jun Zhu. Riflex: A free lunch for length extrapolation in video diffusion transformers. *arXiv* preprint arXiv:2502.15894, 2025. 2
- [130] Wenliang Zhao, Lujia Bai, Yongming Rao, Jie Zhou, and Jiwen Lu. Unipc: A unified predictor-corrector framework for fast sampling of diffusion models. *NeurIPS*, 2023. 2
- [131] Kaiwen Zheng, Cheng Lu, Jianfei Chen, and Jun Zhu. Dpm-solver-v3: Improved diffusion ode solver with empirical model statistics. Advances in Neural Information Processing Systems, 36:55502–55542, 2023. 2
- [132] Zangwei Zheng, Xiangyu Peng, Tianji Yang, Chenhui Shen, Shenggui Li, Hongxin Liu, Yukun Zhou, Tianyi Li, and Yang You. Open-sora: Democratizing efficient video production for all. arXiv preprint arXiv:2412.20404, 2024.
- [133] Xiaofei Zhou, Songhe Wu, Ran Shi, Bolun Zheng, Shuai Wang, Haibing Yin, Jiyong Zhang, and Chenggang Yan. Transformer-based multi-scale feature integration network for video saliency prediction. *IEEE Transactions on Circuits and Systems for Video Technology*, 33(12):7696–7707, 2023. 20
- [134] Le Zhuo, Ruoyi Du, Han Xiao, Yangguang Li, Dongyang Liu, Rongjie Huang, Wenze Liu, Xiangyang Zhu, Fu-Yun Wang, Zhanyu Ma, et al. Lumina-next: Making lumina-t2x stronger and faster with next-dit. Advances in Neural Information Processing Systems, 37:131278–131315, 2024. 1, 2
- [135] Chang Zou, Xuyang Liu, Ting Liu, Siteng Huang, and Linfeng Zhang. Accelerating diffusion transformers with token-wise feature caching. arXiv preprint arXiv:2410.05317, 2024. 2, 17, 18

One Attention, One Scale: Phase-Aligned Rotary Positional Embeddings for Mixed-Resolution Diffusion Transformer

Supplementary Material

In Sec. A, we present the derivation of Equation 6 from the main text. In Sec. B, we provide additional analyses, qualitative results, comparisons, ablations, and overhead breakdowns. Sec. C details further experimental settings, while Sec. D explains the background concepts used throughout the paper. Sec. E presents a discussion of limitations. In Sec. F, we list the prompts used to generate qualitative results. We also include a supplementary video for comparisons on text-to-video generation.

A. Derivation of Equation 6

Intuition. RoPE works by rotating every 2D pair of query and key features by an angle proportional to their positions. When we compute the dot product between these rotated vectors, the rotation angles appear inside cosine and sine terms. As a result, the RoPE-modulated attention score for a single pair behaves like a single sinusoid in the relative offset $\Delta = p_k - p_q$. Summing over all rotary pairs yields a mixture of sinusoids at the predefined RoPE frequencies. This means that the attention score as a function of Δ is effectively a multi-frequency positional kernel whose amplitudes and phase shifts depend on the token content (q, k), while the frequencies are fixed by RoPE. This structure is what we make explicit below.

Derivation. Consider a single attention head with dimensionality d equipped with RoPE. RoPE associates each coordinate pair (2i, 2i+1), $i \in \{0, \dots, d/2-1\}$, with an angular frequency ω_i . For a scalar position $p \in \mathbb{R}$, the i-th 2D subvector is rotated by angle $\theta_i(p) = \omega_i p$ using the 2×2 rotation

$$R(\theta) = \begin{bmatrix} \cos \theta & -\sin \theta \\ \sin \theta & \cos \theta \end{bmatrix}.$$

Splitting $q, k \in \mathbb{R}^d$ into 2D pairs

$$q_i = \begin{bmatrix} q_{2i} \\ q_{2i+1} \end{bmatrix}, \quad k_i = \begin{bmatrix} k_{2i} \\ k_{2i+1} \end{bmatrix},$$

the RoPE relative-position property (Eq. (3) in the main text) implies that the pre-softmax score between a query at position p_q and a key at position p_k depends on the relative offset $\Delta=p_k-p_q$ and can be written as

$$score(q, k, \Delta) = \sum_{i} q_i^{\top} R(\omega_i \Delta) k_i.$$

Expanding each term yields

$$q_i^{\top} R(\omega_i \Delta) k_i = A_i(q, k) \cos(\omega_i \Delta) + B_i(q, k) \sin(\omega_i \Delta),$$

where

$$A_i(q, k) = q_{2i}k_{2i} + q_{2i+1}k_{2i+1},$$

$$B_i(q, k) = q_{2i+1}k_{2i} - q_{2i}k_{2i+1}.$$

Convert to amplitude-phase form by defining

$$C_i(q, k) = \sqrt{A_i(q, k)^2 + B_i(q, k)^2} \ge 0,$$

 $\phi_i = \operatorname{atan2}(-B_i(q, k), A_i(q, k)),$

so that:

$$A_i \cos(\omega_i \Delta) + B_i \sin(\omega_i \Delta) = C_i(q, k) \cos(\omega_i \Delta + \phi_i).$$

Summing over *i* gives

$$score(q, k, \Delta) = \sum_{i} C_i(q, k) \cos(\omega_i \Delta + \phi_i),$$

which motivates the expected-score kernel approximation used in Equation 6 of the main text.

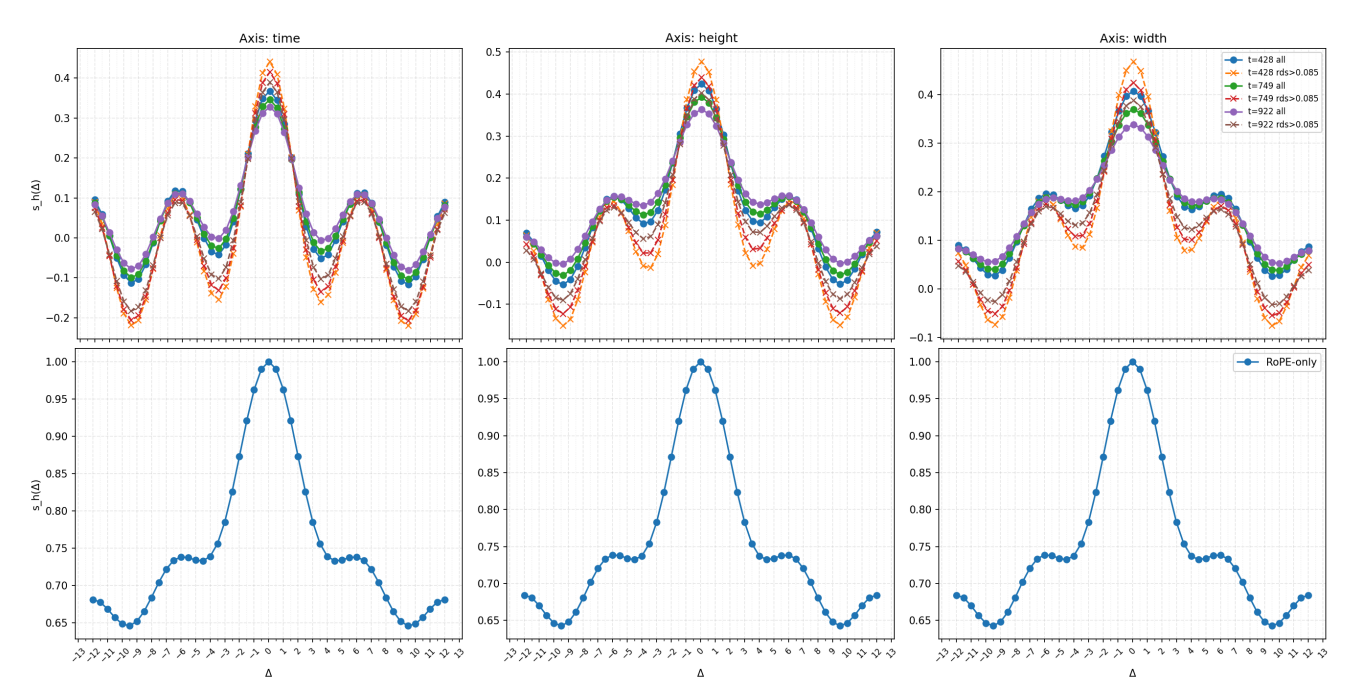


Figure 11. **RoPE-only** Δ **curves.** For comparison with the trained model (Fig. 3 in the main text - replotted as the first row in this figure), we plot in the second row the score-offset curves produced by RoPE alone, *i.e.*, without any influence from token content or attention-head weights. Each curve is a pure superposition of the sinusoidal frequencies defined by RoPE. We observe that the trained model significantly alters the frequency composition compared to the RoPE-only scenario, exhibiting different value ranges, magnitudes, and strengths of peaks and troughs. Moreover, along different axes, *i.e.*, time versus height/width, the nature of these changes differs substantially.

B. Additional Results and Analyses

RoPE-only Δ curve. To isolate the positional behavior imposed by RoPE itself, we compute the Δ -score curve using only RoPE rotations, without any contribution from token content or learned attention weights. We plot this in Fig. 11. This produces a fixed multi-frequency sinusoidal profile reflecting RoPE's predefined frequency schedule. This curve serves as a structural baseline: in the trained model (Fig. 3 in the main text), attention heads reshape this profile substantially— amplifying or suppressing specific frequencies and altering the relative peak magnitudes. In other words, each head develops preferences for particular phase increments that reflect regularities in the training data (e.g., common spatial offsets or geometric patterns). Mixed-resolution interpolation disrupts these learned phase preferences by introducing incompatible phase increments, leading to aliasing and unstable attention, which motivates the need for phase-aligned attention.

Additional qualitative results. In Fig. 12, we provide additional qualitative comparisons between our method and other RoPE interpolation methods when applied to mixed-resolution denoising on FLUX [53]. In the supplementary video, we include comparisons on text-to-video generation for mixed-resolution denoising, using the Wan2.1-1.3B model [109] as the base diffusion model.

Combination with orthogonal diffusion acceleration methods. As shown in Tab. 4 and Tab. 5, our approach integrates seamlessly with orthogonal diffusion acceleration techniques, enabling further reductions in inference time while maintaining comparable generation quality.

Additional use case. In Fig. 13, we show that our method has the potential to make selected regions reach ultra-high resolution while other areas remain low resolution. We use Wan2.1-14B [109], with the low-resolution region set to 480p and the ultra-high-resolution region set to 1920p.

Method		DOVER		1	Time (s)		
	Aesthetic	Technical	Overall	Quality	Semantics	Total	(-)
Ours	99.63	10.01	75.34	0.808	0.622	0.770	43 (1.0×)
+ TeaCache [61]	99.59	10.05	75.34	0.803	0.613	0.765	24 (1.8×)
+ MagCache [75]	99.63	10.10	75.57	0.804	0.619	0.767	22 (2.0×)

Table 4. **Text-to-video results for combination with diffusion acceleration methods.** We show text-to-video results by integrating our method with orthogonal diffusion acceleration techniques. Evaluation is conducted on Wan2.1-1.3B [109] with 50 total steps, including 15 low-resolution steps and a high-resolution token ratio of 0.15. Higher values indicate better performance except for generation time.

Method	FID↓	CLIP-IQA↑	MUSIQ ↑	CLIP↑	Time (s) \downarrow
Ours	31.28	0.623	71.81	31.28	2.8 (1.0×)
+ TeaCache [61]	31.87	0.591	70.72	31.30	$1.9 (1.5 \times)$
+ MagCache [75]	32.76	0.577	70.42	31.34	$1.7 (1.6 \times)$

Table 5. **Text-to-image results for combination with diffusion acceleration methods.** We show text-to-image generation results by integrating our method with orthogonal diffusion acceleration techniques. Evaluation is conducted on FLUX.1-dev [53] with 15 total steps, including 5 low-resolution steps and a high-resolution token ratio of 0.6.

Additional comparisons. In Tab. 6, we fix the compute budget and compare, under different budgets, mixed-resolution and full-resolution denoising performance. We find that FID is particularly sensitive to grainy artifacts that appear when using fewer steps on the FLUX model (7 steps, 30.6 vs. 50 steps, 32.7), so we use more informative metrics such as CLIP-IQA [110] and MUSIQ [47].

In Tab. 7, we provide additional comparisons for the three-stage setting (coarse, mixed, and fine) between our method, Bottleneck Sampling [104], and ToCa [135]. For completeness, we also include the results of RALU [42], which were already reported in the main text. Bottleneck Sampling [104] is a training-free acceleration technique that performs high-low-high resolution denoising with noise reintroduction and scheduler re-shifting. We set the number of inference steps for each stage to N = [4, 10, 5] for $4 \times$ acceleration and N = [2, 7, 3] for $7 \times$ acceleration when applied to FLUX. ToCa [135] is a DiT acceleration method that selectively caches token features based on their importance. We set N = 18 for $4 \times$ acceleration and N = 8 for $7 \times$ acceleration when applied to FLUX. All other settings are the same as in the default ToCa configuration.

Latency (s)	CLIP-	IQA ↑	MUS	SIQ ↑	CLIP↑		
Lucine j (b)	HR Ours		HR	Ours	HR	Ours	
1.6	0.484	0.563	62.85	68.42	31.2	31.4	
2.1	0.538	0.597	66.73	70.31	31.3	31.4	
2.7	0.588	0.623	68.94	71.81	31.2	31.3	
4.1	0.640	0.642	71.48	72.79	31.0	31.3	

Table 6. We compare our mixed-resolution denoising approach with full-resolution (HR) denoising under matched compute budgets on FLUX [53]. The HR baselines use 7, 9, 12, 18 denoising steps. To match the reference latency, we adjust the total number of inference steps in our method to 9, 11, 15, 21, with high-resolution token ratios around 0.6.

Additional ablation. In Tab. 8, we present a quantitative comparison of our method with and without the proposed Boundary Expand-and-Replace procedure.

Overhead of each component. In Tab. 9, we report the overhead incurred by each component in our method, including Cross-Resolution Phase-Aligned Attention (CRPA), the tiny VAE [5], the saliency model [60], and the latent up/downsampler.

Accel.	Method	FID↓	CLIP-IQA↑	MUSIQ ↑	CLIP↑	Latency (s) ↓
_	FLUX-50	32.67	0.647	71.90	30.8	11.5
4×	RALU [42]	32.91	0.556	69.87	31.0	2.7
	Bottleneck [104]	34.01	0.485	65.29	31.1	2.9
	ToCa [135]	31.58	0.498	66.49	31.4	2.9
	Ours	32.45	0.601	72.22	31.2	2.8
7×	RALU [42]	40.49	0.540	60.03	30.8	1.7
	Bottleneck [104]	<u>39.97</u>	0.424	58.34	31.2	1.7
	ToCa [135]	78.82	0.435	50.23	31.0	1.7
	Ours	32.08	0.575	67.35	31.3	1.7

Table 7. Additional comparisons of three-stage inference (coarse, mixed, fine) on FLUX [53], evaluating our method against Bottleneck Sampling [104], ToCa [135], and RALU [42] under $4 \times$ and $7 \times$ acceleration settings.

n_{pad}			DOVER		VBench					
LR	HR	Aesthetic	Technical	Overall	Quality Semantics Total					
0	0	98.90	8.94	68.43	0.781	0.614	0.747			
2	2	99.63	10.01	75.34	0.808	0.622	0.770			
2	4	99.62	9.88	75.18	0.807	0.618	0.769			

Table 8. Ablation study across different overlapping boundary band sizes on Wan 2.1 [109] for text-to-video generation. Here, $n_{\rm pad}$ denotes the overlapping boundary band size for low (LR) and high resolution (HR). With our Boundary Expand-and-Replace procedure, results improve compared to those obtained without it (0,0). We found (2,2) to be a reasonable setting. We evaluate using DOVER [117] and VBench [39], where higher scores indicate better results.

Component	Latency (s)	Percentage
Ours (total)	43	-
CRPA	0.137	0.3%
Tiny VAE [5]	0.030	0.07%
Saliency model [60]	0.273	0.6%
Latent up/down sampler	1.3	2.9%

Table 9. We report the overhead of each component in our method. Evaluation is conducted on Wan2.1-1.3B [109] with 50 total steps, including 15 low-resolution steps and a high-resolution token ratio of 0.15.

Importance-based region selection. In Fig. 14, we show the low-resolution generations at early timesteps, along with the important regions identified by saliency prediction that will be upsampled into high-resolution tokens.

Detailed VBench results. In Tab. 10, we show detailed quantitative evaluation results on VBench [39] when applying different RoPE interpolation methods to the Wan model [109], corresponding to Table 1 in the main text.

C. Additional Experimental Settings

Metrics. For video generation evaluation, we follow VBench [39] and generate using the full set of prompts provided in the benchmark. We also use the reference-free metric DOVER [117] to evaluate these videos and report the corresponding DOVER metrics. For image generation evaluation, we report FID [37], MUSIQ [47], CLIP-IQA [110], and CLIP score [86] on the MSCOCO 2014 validation dataset [58], using 5K randomly sampled image—caption pairs.

Method	Scene	Temporal Style	Overall Consistency	Human Action	Temporal Flickering	Motion Smoothness	Dynamic Degree	Spatial Relationship	Appearance Style	Subject Consistency	Background Consistency	Aesthetic Quality	Imaging Quality	Object Class	Multiple Objects	Color	Time
HR	22.82	22.35	22.19	73.00	99.25	98.92	23.61	67.39	20.10	94.94	97.67	63.54	59.41	62.90	51.14	85.81	172 s
LR+HR	19.48	22.04	22.41	73.00	99.58	98.09	47.22	42.92	20.71	94.08	96.03	61.25	56.77	69.46	45.27	84.87	131 s
PI-LR [13]	19.62	20.78	21.40	69.00	99.59	97.92	45.83	35.11	21.32	92.72	96.02	49.13	42.80	64.40	23.48	87.93	43 s
PI-HR [13]	8.50	19.09	20.88	67.00	97.33	94.44	26.39	22.92	22.01	90.34	94.07	48.62	40.38	55.14	23.86	78.60	
NTK [78]	12.57	19.63	21.59	69.00	97.98	95.27	27.78	31.23	22.17	90.71	94.02	50.22	42.37	59.26	28.43	82.34	
PI+NTK	13.23	21.01	22.20	71.00	99.55	97.35	36.11	40.75	21.69	91.86	95.14	52.78	46.16	61.31	30.64	90.41	
YARN [79]	18.24	21.02	22.67	71.00	99.35	97.62	36.11	39.20	21.94	91.64	94.40	53.63	51.28	65.19	32.70	83.39	
Ours	21.08	22.31	23.04	70.00	99.59	97.65	48.61	52.76	21.03	93.59	95.75	60.70	61.48	74.13	47.64	91.23	43 s

Table 10. Detailed quantitative evaluation results on VBench [39], corresponding to Table 1 in the main text. The % symbol is omitted.

Additional implementation details. For video diffusion with the Wan2.1 model [109], we use 15 denoising steps at 480p and 35 mixed-resolution steps, with a high-resolution token ratio of 15% during the mixed-resolution stage and a CFG scale of 5.0, to generate 49-frame videos. In the hybrid linear and NTK-aware interpolation configuration (PI+NTK) reported in Table 1 of the main text, the linear position scaling factor is set to 1.5, while the NTK scaling factor is set to 1.333.

For image generation in the two-stage setting with FLUX.1-dev [53], we use 18 denoising steps: 7 steps at 512 and 11 mixed-resolution steps, with a 30% high-resolution token ratio and a CFG scale of 3.5.

Our latent up/downsampler for Wan2.1 is a 3D convolutional network with 3 residual blocks and one upsampling or downsampling layer, with hidden dimension 384 and about 25M parameters for each resizer model. Our latent up/downsampler for FLUX is a 2D convolutional network with 20 residual blocks and one upsampling or downsampling layer, with hidden dimension 128 and about 6M parameters for each resizer model.

D. Additional Backgrounds and Definitions

RoPE-dominance score (rds). Following [15], we define the RoPE-dominance score (rds) for an attention head as the average alignment between the pairwise RoPE subspaces of its query (or key) weights. For a head h with weight matrix $W^{(h)} \in \mathbb{R}^{d_h \times d_{\text{model}}}$, RoPE groups dimensions into d/2 rotary pairs (2i, 2i+1). For the i-th pair we consider the corresponding row vectors $W_{2i}^{(h)}$, $W_{2i+1}^{(h)}$ and define

$$\cos \alpha_i^{(h)} = \frac{\langle W_{2i}^{(h)}, W_{2i+1}^{(h)} \rangle}{\|W_{2i}^{(h)}\| \|W_{2i+1}^{(h)}\|}.$$

The RoPE dominance score of head h is then

$$rds^{(h)} = \frac{2}{d} \sum_{i=0}^{d/2-1} |\cos \alpha_i^{(h)}|.$$

Heads with large $rds^{(h)}$ are position-dominated, while heads with small $rds^{(h)}$ are token-content-dominated (their RoPE subspaces vary strongly with the input).

NTK-aware scaling of RoPE (NTK). NTK [78] parameterization can be understood as a frequency-rescaling of RoPE that preserves the precision of high-frequency components while scaling the low-frequency components to accommodate longer sequence lengths. NTK modifies the RoPE frequencies according to:

$$\omega_i' = (\lambda \cdot 10000)^{-2i/d}, \qquad \lambda = s^{d/(d-2)},$$

where $i = 0, \ldots, d/2 - 1$ and s = L'/L.

YaRN. YaRN [79] proposes a detailed scheme for modifying the RoPE frequencies and rescaling the attention logits. In empirical evaluations, it achieves stronger training-free extrapolation than NTK and attains high performance on longer sequences with only modest fine-tuning on the target context length. First, YaRN partitions all frequencies into three regions according to how many cycles they complete over the training length, quantified by

$$r_i = \frac{L \,\omega_i}{2\pi}, \qquad i = 0, \dots, \frac{d}{2} - 1.$$

Given two fixed thresholds α , β satisfying

$$r_{d/2-1} \le \alpha < \beta \le r_0,$$

YaRN updates the RoPE frequencies via

$$\omega_i' = \gamma(r_i) \,\omega_i + (1 - \gamma(r_i)) \,\frac{\omega_i}{s},$$

where the interpolation coefficient $\gamma(r_i)$ is defined piecewise as

$$\gamma(r_i) = \begin{cases} 1, & \text{if } r_i > \beta, \\ 0, & \text{if } r_i < \alpha, \\ \frac{r_i - \alpha}{\beta - \alpha}, & \text{otherwise.} \end{cases}$$

In addition, YaRN applies an attention scaling to stabilize training-free extrapolation at long context lengths. Let A denote the usual (pre-softmax) attention logits matrix and let $\tau > 0$ be a temperature parameter. YaRN replaces A by

$$A' = \frac{A}{\tau},$$

that is, it evaluates the attention weights as

$$\operatorname{Attn}(Q, K, V) = \operatorname{softmax}\left(\frac{A}{\tau}\right) V,$$

with τ chosen to balance the sharpness of attention between the original and extrapolated context lengths.

Saliency prediction. Saliency prediction aims to model human visual attention on images, evolving from early biologically inspired, bottom-up hand-crafted feature models [35, 40, 48, 127] to deep learning approaches facilitated by large datasets such as SALICON [44]. Leveraging pretrained CNNs, models such as DeepGaze I [50, 52], VGG-based architectures [17, 51, 94, 112], and LSTM-enhanced methods [18, 62, 113] achieved substantial improvements, with later works combining multiple backbones [43, 59]. Recent transformer-based models [23, 106] further advance the field by capturing long-range context for both image and video saliency prediction [64, 71, 133].

E. Discussion and Limitations

Although our method achieves strong results in mixed-resolution inference and shows potential to simultaneously handle low-resolution and ultra-high-resolution regions, we observe that the fine details in the ultra-high-resolution areas can be unstable. We attribute this to the underlying diffusion models not being trained on ultra-high-resolution (*e.g.*, 2K or 4K) images or videos. Integrating our method with recent research on ultra-high-resolution generation [49, 84, 85, 107, 119] is an interesting direction for future work, especially for applications such as e-commerce where fine details (*e.g.*, logos or text) must remain highly legible.

F. Prompts

We provide the prompts used to generate the qualitative results shown in the paper but not included in the figures. Prompts for Figure 7 in the main text.

- A pile of oranges in crates topped with yellow bananas.
- A group of baseball players is crowded at the mound.

- A picture of a dog laying on the ground.
- A man holding a camera up over his left shoulder.
- A chicken sandwich in a wrapper near a cell phone.
- There is a small bus with several people standing next to it.

Prompts for Figure 8 in the main text.

- Young man holding a tennis racket while standing in front of a fence.
- Two and a half hotdogs on paper plates are on a counter.
- A red and white fire hydrant is sitting by a curb.

Prompt for Figure 9 in the main text.

• A train going down the tracks that has just gone under a bridge.

Prompt for Fig. 12.

- Blue dishes sitting on a shelf with a plant and flowers.
- A large white bowl of many green apples.
- A modern sink is on top of a bathroom counter top.
- A woman holding her umbrella in her hands.

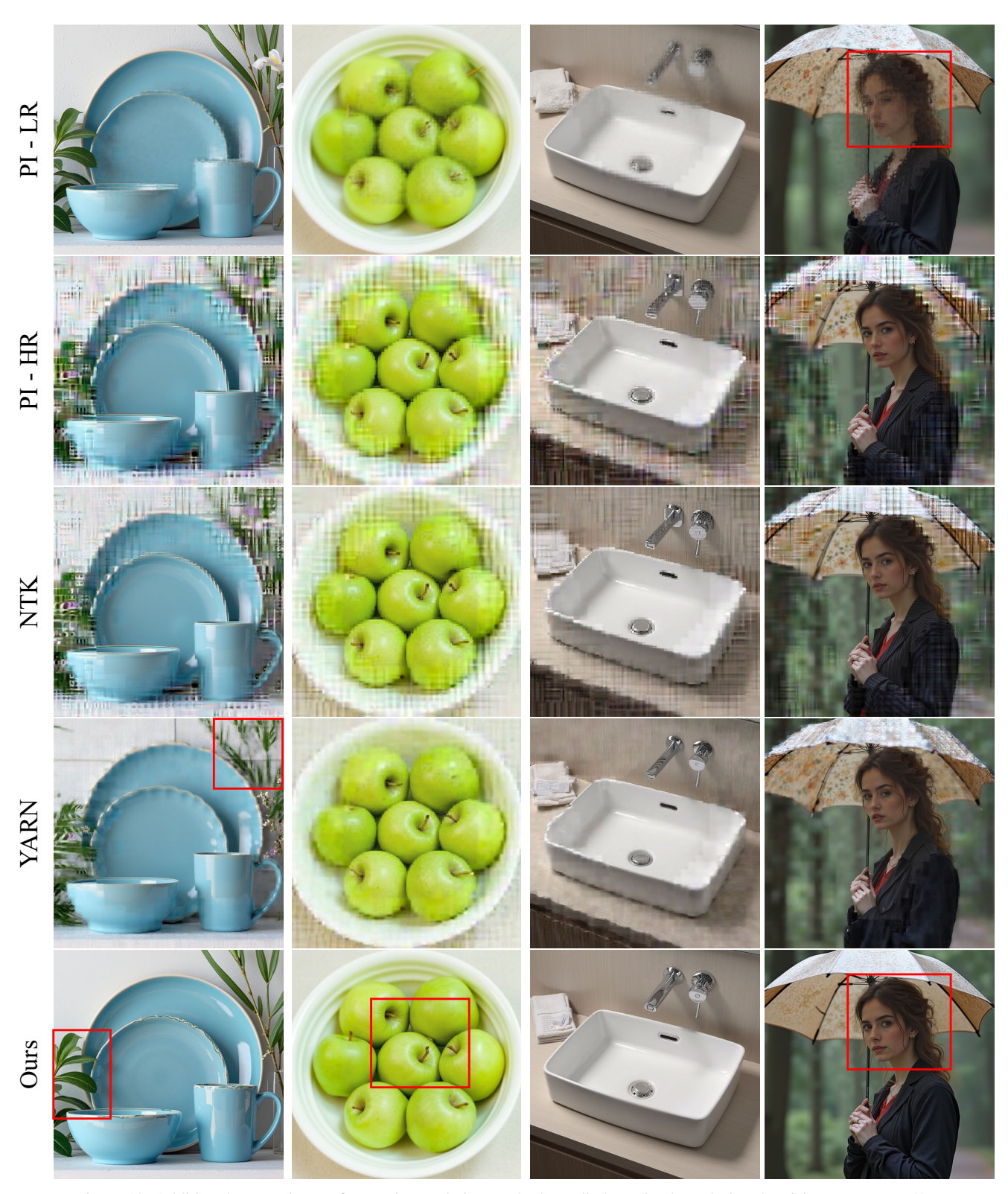


Figure 12. Additional comparisons of RoPE interpolation methods applied to mixed-resolution denoising on FLUX [53].

"A blue toy car on a flat surface."

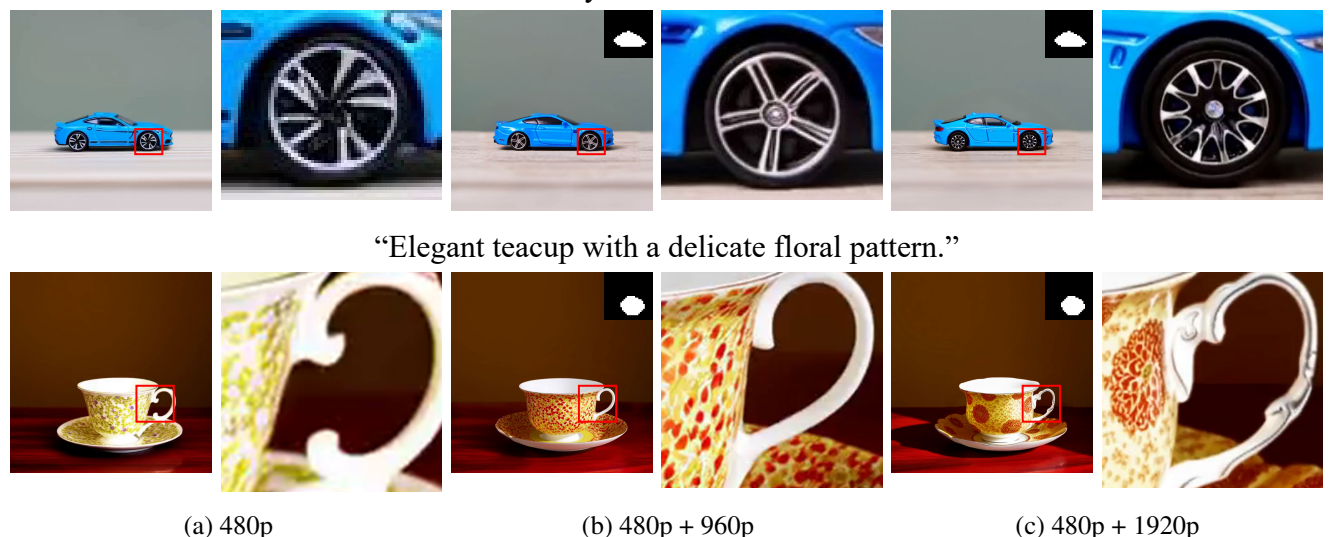


Figure 13. We show that our method enables selected regions to be rendered at ultra-high resolution while the remaining areas stay at lower resolution. Specifically, we present results using the Wan2.1-14B model [109] for: (a) 480×480 only, (b) $480 \times 480 + 960 \times 960$, and (c) $480 \times 480 + 1920 \times 1920$. The high-resolution regions are indicated by the upper-right masks, and we provide zoomed-in views of these areas. As the target resolution increases, the visual quality and level of detail in the high-resolution regions improve, while the overall generation remains consistent.

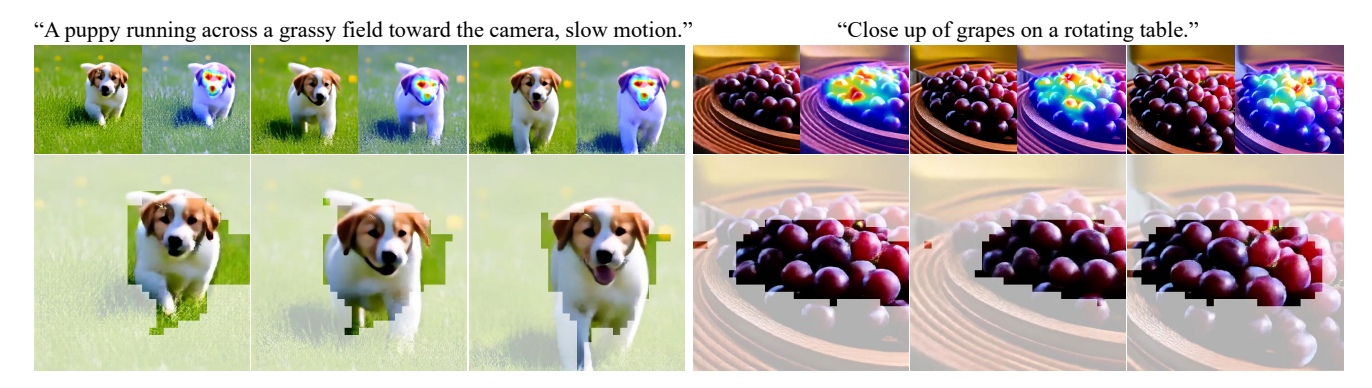


Figure 14. An illustration of our importance-based region selection. Saliency prediction identifies the regions that will be upsampled into high-resolution tokens for mixed-resolution inference. The visualization is based on low-resolution outputs at inference step 15 (out of 50 total steps) using Wan 2.1 [109] for text-to-video generation.